Dry annealing of radiation-damaged zircon: Single-crystal X-ray and Raman spectroscopy study

Martin Ende [a], Chutimun Chanmuang N. [a], Peter W. Reiners [b], Dmitry A. Zamyatin [c], Sarah E. M. Gain [d,e], Richard Wirth [f], Lutz Nasdala [a,*]

[a] *Institut für Mineralogie und Kristallographie, Universität Wien, Althanstr. 14, 1090 Wien, Austria*
[b] *Department of Geosciences, University of Arizona, 1040 4th St., Tucson, AZ 85721, USA*
[c] *Zavaritsky Institute of Geology and Geochemistry, Ural Branch, Russian Academy of Sciences (RAS), Akademika Vonsovskogo Str. 15, 620110 Ekaterinburg, Russia*
[d] *Australian Research Council (ARC) Centre of Excellence for Core to Crust Fluid Systems (CCFS) and ARC National Key Centre for Geochemical Evolution and Metallogeny of Continents (GEMOC), Department of Earth and Planetary Science, Macquarie University, 12 Wally's Walk, North Ryde, NSW 2109, Australia*
[e] *Geological Survey and Resource Strategy Division, Department of Mines, Industry Regulation and Safety, 37 Harris Str., Carlisle, WA 6101, Australia*
[f] *Deutsches GeoForschungsZentrum GFZ, Telegrafenberg, 11473 Potsdam, Germany*

ARTICLE INFO

ABSTRACT

Structural reconstitution upon dry thermal annealing of mildly to strongly radiation-damaged, gem-quality zircon from Sri Lanka has been studied by single-crystal X-ray diffraction and Raman spectroscopy. Results of structure refinement of a strongly radiation-damaged zircon (sample GZ5, calculated alpha dose $\sim 4 \times 10^{18}$ g^{-1}) indicate the existence of an interstitial oxygen site that is sparsely occupied (about 4% of all O atoms). Annealing of this sample at T_a (annealing temperature) = 700 °C has resulted in nearly complete recrystallization of its amorphous volume fraction and significant decrease in the occupation of O-interstitial sites. For all samples studied, annealing up to $T_a \leq 650–700$ °C is characterised by preferred recovery of Raman shifts (compared to Raman FWHMs; full width at half band maximum) and extensive contraction of the unit-cell volume, in particular along unit-cell dimension *a*. This low-*T* annealing is dominated by epitaxial growth of the crystalline volume fraction at the expense of the amorphous volume fraction, and general recovery of low-energy defects. During annealing at $T_a = 700–1400$ °C there is preferred recovery of Raman FWHMs (compared to Raman shifts) and only mild unit-cell contraction. High-*T* annealing is dominated by the recovery of high-energy defects such as recombination of cation Frenkel pairs. Here, unit-cell parameter *a* shows a remarkable behaviour (namely, mild re-increase at $T_a = 700–1150$ °C and mild final shrinking at $T_a = 1000–1400$ °C), which is attributed to enhanced contortion of ZrO$_8$ polyhedrons due to cation repulsion. The combined data set of Raman band and unit-cell parameter presented herein will help analysts to assign Raman spectra of annealed unknowns to certain recovery stages.

1. Introduction

Zircon (ideally ZrSiO$_4$; tetragonal space group $I4_1/amd$) is a mostly accessory, widespread component in igneous, metamorphic, and sedimentary rocks. This mineral commonly incorporates low levels of U and Th at the eight-coordinated Zr^{4+} site in its lattice, whereas Pb is mostly excluded during primary growth (Krogh, 1993). The vast majority of Pb in zircon is therefore radiogenic in nature, formed by the radioactive decay of ^{238}U, ^{235}U and ^{232}Th. Zircon has a high melting temperature and is remarkably robust against near-surface weathering and chemical alteration over a wide range of *p–T* conditions in the lithosphere. This

results in a remarkable ability to retain not only U and Th, but also the radiogenic Pb due to the extremely slow volume diffusion of Pb in zircon (Cherniak and Watson, 2001). The above makes zircon a prime candidate for U–Pb geochronology (Davis et al., 2003). Other applications of zircon in Earth sciences research include (U–Th)/He thermochronology (Ginster et al., 2019; Guenthner et al., 2013; Reiners, 2005), fission-track dating (Gombosi et al., 2014; Montario and Garver, 2009) and petrogenetic studies (Horie et al., 2006; Nasdala et al., 2010; Zamyatin et al., 2017). In materials science research, ZrSiO$_4$-based ceramics have been proposed as repository material for the immobilisation of nuclear waste (Ewing et al., 2003; Weber et al., 1998).

---

* Corresponding author.
E-mail address: lutz.nasdala@univie.ac.at (L. Nasdala).

The radioactive decay of heavy radionuclides – in particular recoils of heavy daughter nuclei upon emission of an alpha particle – involves high-energy ballistic processes that create structural damage to the zircon lattice (Devanathan et al., 2006; Weber et al., 1994). Upon progressive damage accumulation – i.e., provided that no thermal annealing of the damage (Nasdala et al., 2001) or fluid-driven recrystallisation (Geisler et al., 2003; Nasdala et al., 2010) does occur – zircon may eventually be transformed into a fully aperiodic, glassy state (Capitani et al., 2000; Nasdala et al., 2002; Zamyatin et al., 2017) that is referred to as "metamict" (Ewing, 1994; Ewing et al., 2003). Depending on the level of accumulated self-irradiation damage, bulk properties of zircon change appreciably (Chakoumakos et al., 1987; Holland and Gottfried, 1955; Oliver et al., 1994). This in particular applies to general, radiation-damage-induced reduction of the "chemical durability" of zircon, potentially leading to preferred weathering (Fig. 1a), leaching and alteration, fluid-driven recrystallisation (Fig. 1b) and/or loss of the radiogenic Pb from more radiation-damaged samples and interior regions (Corfu, 2013; Geisler et al., 2003; Horie et al., 2006; Krogh and Davis, 1975; Nasdala et al., 2010). The changed bulk properties of radiation-damaged zircon can be "reset" proportionally by partial structural reconstitution through dry annealing. Quantitative estimation of the magnitude of structural recovery, however, is still controversial, as the result will depend strongly on the analytical technique and the particular parameter used (Fig. 2; Nasdala et al., 2004; Mattinson et al., 2007).

One prominent example for the need to understand fractional structural restoration upon dry annealing is the CA–TIMS (chemical abrasion–thermal ionisation mass spectrometry) method (Mattinson, 2005, 2011). This procedure involves a high-T annealing treatment step followed by a partial chemical dissolution step. It aims at improving the concordance of U–Pb geochronology results by removing prior to U–Pb analysis strongly radiation-damaged zircon domains (Fig. 1c) that are more likely affected by secondary Pb loss. Earlier pre-analysis-treatment methods such as air abrasion (Krogh, 1982) or chemical abrasion by leaching in hot (80 °C) HF at ambient pressure (Mattinson, 1994; Mundil et al., 2001), were found to be moderately successful in several cases. In contrast, after thermal annealing, typically for 48–60 h at 900–1000 °C (Huyskens et al., 2016; Mattinson, 2005, 2011), the HF digestion pre-treatment of heterogeneous zircon grains was found to be much more

sensitive to a preferred removal of Pb-loss-affected domains. The CA–TIMS technique is not undisputed and seems to fail in particular for non-heterogeneous zircon samples of elevated radiation damage (Corfu, 2009); it nevertheless has made a great contribution to improving the reliability of U–Pb geochronology results (Corfu, 2009, 2013; Mattinson, 2011; Mundil et al., 2004). The CA–TIMS technique, however, is still fully empirical. Series of experiments have indicated which annealing T and duration (plus which chemical treatment) work best, but the reasons for the efficiacy of the chemical treatment after partial, dry high-T annealing of zircon samples remain unclear (Mattinson, 2011).

Another example for the need to understand dry-annealing processes is the effect of radiation damage on He retention in zircon. Guenthner et al. (2013) showed that He diffusivity in zircon, and therefore the effective closure T of the zircon (U–Th)/He thermochronometer, changes systematically with accumulated damage. Diffusivity decreases, and closure T increases, up to a self-irradiation dose of 2×10^{18} α/g, with opposite relationships at higher radiation doses. This means that realistic interpretations of zircon (U–Th)/He dates require understanding the coupled evolution of He diffusivity and radiation damage accumulation and annealing (e.g., Ginster et al., 2018) as a function of time and temperature. It is therefore crucial to understand (i) the nature and extent of recovery and structural changes in radiation-damaged zircon upon dry heating and (ii) which degrees of recovery and structural changes are estimated by which analytical technique and evaluated by which parameter?

Also, radiation-damaged zircon consists of an aperiodic ("X-ray amorphous") volume fraction and a crystalline volume fraction affected by various densities of defects (Crocombette and Ghaleb, 2001; Trachenko et al., 2002). It has been debated for several decades already which of the two recovers first (that is, at lower T) upon dry annealing. As early as in 1955, Holland and Gottfried concluded that single point defects are in general annealed more easily than highly damaged zircon. Correspondingly, Geisler et al. (2001) assigned a distinct two-step annealing trend observed from Raman spectral changes to low-T recovery of defects in crystalline remnants followed by high-T epitaxial recrystallization of the crystalline remnants at the expense of the aperiodic volume fraction. Nasdala et al. (2001) suggested the opposite, bringing into consideration the fact that, in contrast to epitaxial recrystallization, healing of point defects in the crystalline phase
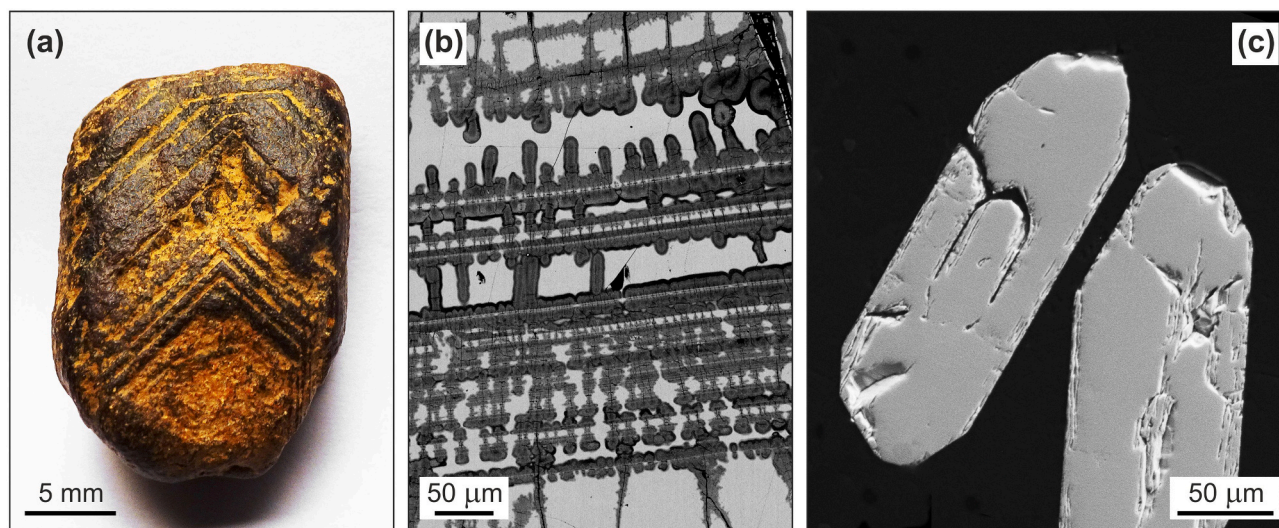

Fig. 1. Images visualising lowered chemical resistance of more radiation-damaged zircon. (a) Strongly radiation-damaged zones in this zircon grain from a placer near Okkampitiya, Sri Lanka, are weathered (ochre) whereas mildly damaged zones (brown) have remained un-attacked. (b) BSE image of a zircon from Bancroft, Ontario, showing chemical alteration (lowered back-scatter intensity) preferentially in more radiation-damaged zones (cf. Nasdala et al., 2010). Image courtesy Dieter Rhede. (c) SE image of two polished zircon grains after several preliminary CA–TIMS steps. Chemical abrasion has "mined out" (Mattinson, 2011) highly radiation-damaged zones from grain interiors. Image courtesy James M. Mattinson. (For interpretation of the references to colour in this figure legend, the reader is referred to the web version of this article.)
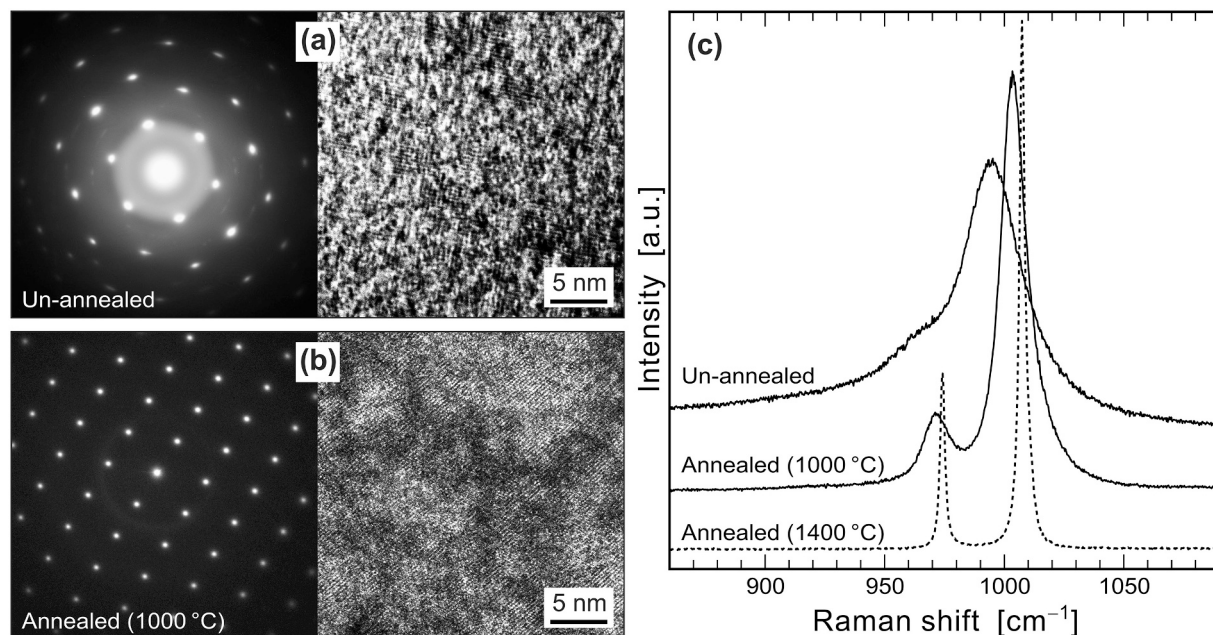
Fig. 2. Apparently incongruent recovery of the long-range order and the short-range order of zircon G3 upon dry annealing (1000 °C; 48 h) prior to CA–TIMS chemical treatment. (a) Pair of TEM electron diffraction pattern (left) and lattice fringe image (right) obtained from the un-annealed sample, both showing evidence of severe radiation damage (including a distinct "amorphous ring" and smeared-out peaks in the diffraction pattern). (b) Analogous pair of TEM images obtained from the sample after annealing at 1000 °C. (c) Plot of Raman spectra in the SiO_4-stretching range, obtained before and after annealing; shown in comparison with the spectrum of the fully annealed sample (1400 °C; 96 h). Spectra are plotted with vertical offset for clarity. Note that annealing at 1000 °C has resulted in decidedly incomplete relaxation of the Raman band broadening whereas TEM images indicate extensive recrystallization.

requires vacancy diffusion and hence comparably high *T*. This seemed to be in accordance with earlier results of Presby and Brown (1974) who found damage in proton-bombarded quartz with low defect density to be stable up to ~750 °C whereas highly damaged regions started to anneal below 250 °C. There is no general agreement thus far on how the thermal regimes of the two major recovery processes – healing of point defects in the crystalline volume fraction and recrystallization of amorphous volume fractions – are related to one another?

We have addressed these questions by subjecting six gem-quality zircon samples to a detailed annealing study in the temperature range 450–1400 °C. The goal of the present work is to describe the *T*-induced recovery process by comparing the results of Raman spectroscopy and single-crystal X-ray diffraction. In addition, laser-induced PL (photoluminescence) spectra were obtained to provide comparability with published data (Lenz and Nasdala, 2015; Nasdala et al., 2018a).

2. Materials and methods

2.1. Samples and preparation

Six gem-quality zircon specimens (GZ2, GZ4, GZ5, GZ8, M127 and M257) were analysed in detail in the present study. Formation and original host rocks of these samples are unknown; all were recovered from placer deposits (i.e., river gravels) in the Ratnapura district, Sabaragamuwa Province, Sri Lanka. The three samples GZ8 (Nasdala et al., 2018b), M127 (Nasdala et al., 2016) and M257 (Nasdala et al., 2008) have already been studied in detail elsewhere, prior to being proposed as reference materials especially for SIMS (secondary ion mass spectrometry) U–Pb geochronology.

In addition, we have included two more samples for comparison. First, the strongly radiation-damaged Sri Lankan zircon sample G3 (Kennedy, 2000; Nasdala et al., 2004) was studied in preliminary experiments (Mattinson et al., 2007). Second, sample R–5 from Phnum Trom, Ratanakiri province, Cambodia (Nasdala et al., 2018a; Zeug et al., 2018) was included as a reference for virtually non-radiation-damaged

natural zircon.

The six gemstones under investigation were cut into ~2–3 mm thick slices with a diamond-coated wire. One slice per sample was polished on one side for EPMA (electron probe micro-analyser), LA–ICP–MS (laser ablation–inductively coupled plasma–mass spectrometry) and Raman and PL spectroscopic measurements of the starting materials. Hand-polishing was done on cloth and did not involve the use of a nonferrous metal disk, to avoid possible Pb contamination. For EPMA analysis, slices were coated with C for conductivity. At least one slice per sample was crushed into small fragments using a stainless-steel cylinder and piston (see Nasdala et al., 2018b). Fragments were hand-picked under a high-magnification optical microscope (plane- and cross-polarised light) for screening inclusions. Fragments with <300 μm longest dimension were selected for single-crystal X-ray analysis. For determination of unit-cell parameters, these fragments were glued to the end of a glass fibre (50 μm diameter). For diffraction-peak and diffuse-scattering analysis, fragments were remounted on Kapton loop sample holders, in order to lower the diffraction background. Other fragments were subjected to (U–Th)/He analysis, after being photographed and measured to get rough volume estimates. For TEM (transmission electron microscopy), thin sections were prepared and, after being detached from the glass slide, ion-beam thinned and subsequently coated with C.

Fragments of 100–500 μm size were selected for dry annealing experiments in a Pt crucible. Note that for zircon annealing, an inert crucible material such as Pt or silica needs to be used. The use of an alumina crucible, in contrast, would be critical as the close proximity of Al_2O_3 may stimulate surficial high-temperature breakdown of zircon and decomposition into oxides (Váczi et al., 2009). In the present study, dry annealing was done by heating nine fragments per zircon sample, each of them at one of nine different temperatures (450, 550, 600, 650, 700, 850, 1000, 1150 and 1400 °C). Annealing was done in ambient atmosphere. The heating rate was ca. 30 °C/min. After a 96-h holding time at the designated temperature, the furnace was switched off and samples were allowed to cool down slowly, before being taken out of the furnace after several hours, at a temperature of less than 100 °C. The fairly long,

four-day annealing time was chosen because it is well known that annealing of radiation-damaged minerals for only a few hours may not suffice to reach near-equilibrium conditions and hence result in incomplete annealing (Ginster et al., 2019; and references therein).

2.2. Analytical methods

Mass densities were determined by repeated weighing of the starting materials in distilled water (with a minute amount of detergent added to decrease surface tension) and in air. The major-element chemical composition was determined by WDX (wavelength-dispersive X-ray spectrometry) using a Cameca SX100 EPMA. The system was operated at 15 kV and 200 nA. Details are reported elsewhere (Zamyatin et al., 2017). Trace element concentrations and U–Pb ages were obtained simultaneously, by LA–ICP–MS analysis carried out using an Agilent 7700× system. Sample material was ablated by a Photon Machines Analyte Excite 193 nm ArF excimer laser (see Jackson et al., 2004). Analyses of unknowns were bracketed by two analyses of NIST SRM–610 (Jochum et al., 2011) at the beginning and end of each run. For more experimental details see Nasdala et al. (2018b). Data reduction and calculation of trace element mass fractions and U–Pb ages were done using the Glitter software package (Griffin et al., 2008). (U–Th)/He ages of zircon samples were determined according to a procedure described in detail elsewhere (Guenthner et al., 2016; Nasdala et al., 2004; Reiners, 2005). As aliquots analysed consisted of small internal fragments originating from large gemstones, no alpha-ejection correction was applied. Electron diffraction patterns and lattice fringe images were obtained by means of a Philips CM200 transmission electron microscope equipped with a Gatan imaging filter. The system was operated at 200 kV and 1 nA. For more experimental details see Wirth et al. (2001).

Raman and PL analyses were conducted by means of a Horiba Lab-RAM HR Evolution system. Raman spectra were excited by a 632.8 nm He–Ne laser (8 mW at the sample surface). Emission spectra were recorded using a 473 nm diode laser (3 mW; to obtain the ~580 nm emission of Dy^{3+}) and a 532 nm, frequency-doubled Nd:YAG laser (10 mW; to obtain the ~860 nm emission of Nd^{3+}). The scattered/emitted light was dispersed using a 1800 grooves/mm diffraction grating, resulting in spectral resolution ranging from 0.7 cm^{-1} (near infrared range) to 0.9 cm^{-1} (yellow range of the electromagnetic spectrum). For further experimental details see Nasdala et al. (2018a) and Zeug et al. (2018). Spectral fitting was done after appropriate background subtraction, assuming combined Lorentzian-Gaussian band and line shapes. Measured FWHM (full width at half maximum) values of spectroscopic signals were corrected for the artefact of experimental band broadening arising from the limited spectral resolution, following the procedure of Váczi (2014).

Single crystal X–ray diffraction was done using two different systems. First, measurements done to obtain unit-cell parameters were conducted for all six samples and all annealing temperatures by means of a Huber 5042 four-circle diffractometer, using Mo–K$\alpha_{1,2}$ radiation. Ten data points were measured for each of the six gem-zircon samples. Bragg peak positions were measured using the peak centring method described by King and Finger (1979) and applied e.g. by Ende et al. (2020). In reducing the data, lattice parameters were constrained to tetragonal symmetry. More details are documented elsewhere (Nasdala et al., 2018b). Second, two-dimensional scanning of individual Bragg reflections and their diffuse-scattering background was done for samples GZ2, GZ4 and GZ5 using a Stoe StadiVari system equipped with air-cooled Incoatec IµS 2.0 Mo micro-focus tube source and Dectris Pilatus 300 K detector. The sample-detector distance and exposure time per frame were set to 180 mm and 33 s (diffraction-peak mapping), and 60 mm and 100 s (diffuse-scattering mapping), respectively. Each sample was first oriented, and then the selected Bragg diffraction peaks (400) and (004) were focused and analysed. For sample GZ5, rocking curves with angular steps of 0.125° in ω-rotational mode with about ±6° in both directions from the Bragg-peak centre were taken, having 2θ and χ

as detector angles. The exposure time was set to 33 s per frame. In order to observe possible diffuse scattering, standard Φ scans (360°; 0.5° step size; 66 s per step; 60 mm sample–detector distance) were done. All analyses were conducted using the Stoe & Cie X-Area (version 1.72) software collection, and data processing was done using the Dectris Albula software (extraction of frames) and the MathWorks Matlab software (integration of frames). Crystal-structure analysis was done for sample GZ5 and its annealed counterparts, using the parameters listed in Table S3 in the ESM (electronic supplementary material). Here, the X-Area software was used for integration and numerical absorption correction. Due to strongly broadened diffraction peaks of GZ5 and the resulting large spots on the diffraction pattern, elliptical masks for integration had to be optimised and increased in size, from ~7 pixels (standard value) to ~23 pixels. Also, integration was done over an enlarged range of the effective mosaic spread (typically 0.005–0.020, here increased to 0.069); which is a combination of the divergence of the primary beam and the mosaic spread of the crystal (Rossmann, 1979). The structure refinement was performed with SHELXL (Sheldrick, 2015).

3. Results

3.1. Characterisation of un-annealed zircon

3.1.1. General characterisation of samples

General parameters of the zircon samples studied (including mass densities, ages, unit-cell dimensions and selected spectroscopic parameters) are summarised in Table 1, and chemical compositions are quoted in Table 2. Results of multiple micro-technique (EPMA, spectroscopy) analyses did not show significant variations within samples. This supports their internal homogeneity, which is a presumption for conducting an annealing study using multiple small chips originating from one original stone.

Time-integrated alpha doses were calculated based on U–Pb ages (Table 1) and present U and Th concentrations (LA–ICP–MS results; Table 2) according to Murakami et al. (1991). For the five samples GZ2 to GZ8, doses are in the range 1.1–2.5 × 10^{18} alpha events per gram, which corresponds to mild to moderate radiation damage well below the first percolation point (for Sri Lankan zircon at ~3.5 × 10^{18} α/g; Salje et al., 1999). This point characterises the level of radiation damage at which amorphous clusters cease to be isolated "islands" and, instead, interconnect to form a three-dimensional network (Salje et al., 1999; Trachenko et al., 2004). The alpha doses calculated for sample GZ5 (~ 4 × 10^{18} α/g) and reference G3 (~ 5 × 10^{18} α/g) lie beyond the percolation point and hence correspond to rather severe radiation damage. These general estimates are supported by analytical data (Table 1; Fig. 3). Mass densities in the range 4.67–4.40 g/cm^3 (cf. Ellsworth et al., 1994; Holland and Gottfried, 1955; Murakami et al., 1991; Vaz and Senftle, 1971; Zhang et al., 2000) and unit-cell volumes of 262–279 Å^3 (cf. Holland and Gottfried, 1955; Nasdala et al., 2004) indicate that structural states of samples range from moderately to strongly radiation-damaged. This is also in agreement with the observed degrees of broadening of Raman (cf. Nasdala et al., 2001; Zhang et al., 2000) and PL spectroscopic signals (cf. Lenz and Nasdala, 2015).

We emphasise that unit-cell parameters quoted in Table 1, and Table S1 in the ESM, were obtained using a peak centering method (King and Finger, 1979) that allows one to evaluate non-symmetric Bragg reflections. In contrast, the application of the standard algorithm that integrates diffraction peaks by peak masking, and assumes the Bragg peak positions in the centres of the masks, yielded $a \sim 6.64$ Å and $c \sim 6.05$ Å for both the un-annealed chips of GZ5 and GZ8. These unit-cell dimensions are considerably lower than values observed with the aforementioned peak centring method. In Fig. S5 it can be seen for the example of (400) Bragg peaks that their centres do not match with the centres of the entire peaks measured. Instead, Bragg-peak maxima are at lower 2θ values (resulting in higher unit-cell parameters), compared to

Table 1
General characterisation of zircon samples, and unit-cell and spectroscopic parameters before annealing and after complete annealing.

Sample	Annealing-T	R–5[a]	GZ2	M257[b]	M127[c]	GZ4	GZ8[d]	GZ5	G3[e]
Sample weight (g)		8.31	0.578	5.14	2.54	0.516	3.85	0.520	(~0.008)
Mass density (g/cm³)		4.674 ± 0.005	4.67 ± 0.01	4.63 ± 0.01	4.625 ± 0.005	4.59 ± 0.01	4.537 ± 0.005	4.395 ± 0.05	n.a.
$^{206}Pb/^{238}U$ age (Ma)		0.92 ± 0.07	530 ± 5	561.3 ± 0.3	524.36 ± 0.16	549 ± 6	543.92 ± 0.06	529 ± 10	542 ± 5
(U–Th)/He age (Ma)		0.87 ± 0.13	480 ± 26	419 ± 6	426 ± 7	476 ± 13	426 ± 9	446 ± 21	441 ± 21
Calculated alpha dose (×10¹⁸ /g)		0.0004	1.11 ± 0.18	1.70 ± 0.04	1.82 ± 0.06	2.27 ± 0.17	2.53 ± 0.11	3.97 ± 0.20	5.01 ± 0.24
Unit-cell dimension a (Å)	Un-annealed	6.6037(1)	6.6060(2)	6.6250(3)	6.6397(2)	6.6457(2)	6.6722(7)	6.749(3)	n.d.
	1400 °C	6.6038(1)	6.6034(1)	6.6041(1)	6.6043(1)	6.6044(1)	6.6043(2)	6.6052(1)	6.6051(3)
Unit-cell dimension c (Å)	Un-annealed	5.9789(2)	6.0059(4)	6.0286(5)	6.0360(4)	6.0475(4)	6.0678(9)	6.119(4)	n.d.
	1400 °C	5.9791(1)	5.9791(2)	5.9801(2)	5.9790(3)	5.9794(1)	5.9806(4)	5.9797(2)	5.9819(5)
Unit-cell volume (Å³)	Un-annealed	260.73(1)	262.09(3)	264.60(3)	266.10(2)	267.09(3)	270.26(8)	278.7(3)	n.d.
	1400 °C	260.75(1)	260.72(1)	260.81(1)	260.78(2)	260.81(1)	260.98(2)	260.88(1)	260.97(4)
Raman shift (cm⁻¹)[f]	Un-annealed	1007.6 ± 0.5	1004.7 ± 0.5	1001.0 ± 0.5	999.4 ± 0.5	998.2 ± 0.5	996.6 ± 0.5	994.9 ± 0.5	996.2 ± 0.5
	1400 °C	1007.6 ± 0.5	1008.1 ± 0.5	1007.8 ± 0.5	1007.1 ± 0.5	1007.8 ± 0.5	1007.6 ± 0.5	1007.7 ± 0.5	1007.5 ± 0.5
Raman FWHM (cm⁻¹)[f]	Un-annealed	1.8 ± 0.2	7.0 ± 0.5	11.6 ± 0.8	14.0 ± 1.1	17.8 ± 1.3	21.1 ± 1.6	29.2 ± 2.0	30.4 ± 2.5
	1400 °C	1.8 ± 0.2	1.8 ± 0.2	1.9 ± 0.2	2.0 ± 0.3	2.2 ± 0.3	2.1 ± 0.3	2.6 ± 0.3	2.5 ± 0.4
Dy³⁺ FWHM (cm⁻¹)[g]	Un-annealed	10 ± 1	23 ± 2	36 ± 3	44 ± 4	55 ± 5	68 ± 7	80 ± 8	87 ± 5
	1400 °C	10 ± 1	11 ± 1	12 ± 1	12 ± 1	12 ± 1	12 ± 1	13 ± 1	14 ± 1
Nd³⁺ FWHM (cm⁻¹)[h]	Un-annealed	14 ± 1	26 ± 2	33 ± 3	36 ± 4	38 ± 4	40 ± 4	52 ± 7	51 ± 5
	1400 °C	14 ± 1	14 ± 1	15 ± 1	15 ± 1	15 ± 1	16 ± 1	21 ± 2	22 ± 3

Notes: Data for all annealing temperatures are quoted in Table S1 in the ESM. n.a. = not analysed (sample G3 was not included in mass density measurements because of insufficient amount of material). n.d. = not determined (Bragg reflections asymmetric, too low in intensity and obscured by diffuse scattering).

[a] Mass density and $^{206}Pb/^{238}U$ age of R–5 from Zeug et al. (2018) and Nasdala et al. (2018a).
[b] Mass density and $^{206}Pb/^{238}U$ and (U–Th)/He ages of M257 from Nasdala et al. (2008).
[c] Mass density and $^{206}Pb/^{238}U$ and (U–Th)/He ages of M127 from Nasdala et al. (2016).
[d] Mass density and $^{206}Pb/^{238}U$ and (U–Th)/He ages of GZ8 from Nasdala et al. (2018b).
[e] Only a small fraction of the original sample was available for, and included in, the present study. $^{206}Pb/^{238}U$ age of G3 from Kennedy (2000). (U–Th)/He age from Nasdala et al. (2004).
[f] Quoted for the $\nu_3(SiO_4)$ Raman band.
[g] Quoted for the 17,210 cm⁻¹ line of Dy³⁺.
[h] Quoted for the 11,360 cm⁻¹ line of Nd³⁺.

centres of entire masked peaks. Consequently, application of the standard algorithm would have resulted in too low unit-cell parameters for zircon samples with elevated levels of radiation damage.

It needs to be considered cautiously that parameter changes of Sri Lankan zircon do not coincide directly with the calculated alpha doses. Owing to the particular thermal annealing history, Sri Lankan gem zircon has retained only about 55% of the self-irradiation damage experienced since the time of closure of the U–Pb system (Nasdala et al., 2004). This prevents direct comparability of their dose-to-parameter-change relationships with that of samples of other origin. For the purposes of the present study, it is important to note that analytical data of all samples investigated plot well within the "Sri Lankan tends" of parameter changes upon self-irradiation (Fig. 3). Significant mismatches, in contrast, would have indicated an unusual post-growth thermal history, such as caused by thermal treatment for colour enhancement (a common practice of Sri Lankan gem miners and dealers).

3.1.2. Structure refinement of zircon GZ5

Structure-refinement results are presented in Table S3, atomic coordinates are quoted in Table S4, and anisotropic displacement parameters are contained in Table S5. A sketch of the structure of the severely radiation-damaged zircon GZ5, in comparison with structures of two published references (virtually non-damaged and moderately damaged) is presented in Fig. 4.

3.2. Characterisation of annealed zircon

3.2.1. Raman and PL spectroscopy

Spectroscopic and unit-cell data of the fully annealed samples (1400 °C; 96 h) are presented in Table 1, and parameters for all nine annealing temperatures T_a are provided in Table S1 in the ESM. Example Raman spectra are shown in Figs. 2c and S2, and selected PL spectra, obtained in the yellow and near-infrared ranges of the electromagnetic spectrum, are presented in Fig. S2. Raman bands are assigned to internal anti-symmetric (~ 1008 cm⁻¹) and symmetric (~ 974 cm⁻¹) stretching vibrations of SiO₄ units. The analysed groups of lines in PL spectra are assigned to crystal-field-split electronic transitions of trivalent ions of REE (rare-earth elements). These include the $^4F_{9/2} \to {}^6H_{13/2}$ transition of Dy³⁺ near 17,400 cm⁻¹ (or ~ 575 nm wavelength; yellow) and the $^4F_{3/2} \to {}^4I_{9/2}$ transition of Nd³⁺ near 11,400 cm⁻¹ (or ~ 877 nm wavelength; near infrared). Emissions of Sm³⁺, Pr³⁺ and Tm³⁺ were detected as well, but spectra were not obtained. For the latter REEs, fitting results must remain unreliable because emissions consist of numerous lines that superimpose each other (discussed in more detail by Lenz and Nasdala, 2015). All Raman bands and PL lines show significant decreases of widths upon annealing. Raman bands exhibit notable up-shifts to higher Raman-shift values, whereas individual Stark lines in PL spectra shift somewhat towards lower wavenumbers (Fig. S2).

In the plot of spectral position versus width of the main Raman band (Fig. 5) it can be seen that the two parameters do not recover consistently. Rather, there are two consecutive trends of parameter changes; this observation is consistent with earlier findings (Geisler et al., 2001). Up to T_a ~ 650–700 °C there is preferred Raman-shift increase, which becomes less pronounced at higher T_a. The resulting "bend" in the

Table 2

Chemical compositions (major oxides, EPMA results; trace elements, LA–ICP–MS results) of zircon samples.

Oxide/element	Isotope measured	R–5[a]	GZ2	M257[b]	M127[c]	GZ4	GZ8[d]	GZ5	G3[e]
Major oxides (wt%):		(n = 172)	(n = 15)	(n = 76)	(n = 63)	(n = 18)	(n = 84)	(n = 29)	(n = 6)
SiO$_2$	–	34.2 ± 0.2	32.2 ± 0.4	32.7 ± 0.1	32.6 ± 0.2	32.2 ± 0.4	32.5 ± 0.2	31.5 ± 0.4	32.6 ± 0.1
P$_2$O$_5$	–	b.d.l.	b.d.l.	b.d.l.	0.057 ± 0.006	0.035 ± 0.013	0.022 ± 0.003	0.040 ± 0.009	0.147 ± 0.006
Y$_2$O$_3$	–	0.042 ± 0.009	b.d.l.	0.019 ± 0.005	0.109 ± 0.012	0.0568 ± 0.007	0.059 ± 0.005	0.180 ± 0.008	0.172 ± 0.004
ZrO$_2$	–	66.8 ± 0.3	64.7 ± 0.3	66.4 ± 0.2	65.9 ± 0.3	64.6 ± 0.2	66.5 ± 0.2	64.5 ± 0.3	64.3 ± 0.2
Yb$_2$O$_3$	–	b.d.l.	b.d.l.	b.d.l.	0.028 ± 0.012	b.d.l.	0.012 ± 0.003	0.030 ± 0.003	0.044 ± 0.004
HfO$_2$	–	0.693 ± 0.035	2.21 ± 0.25	1.38 ± 0.01	1.50 ± 0.02	1.60 ± 0.04	1.39 ± 0.02	1.83 ± 0.02	1.82 ± 0.01
ThO$_2$	–	b.d.l.	0.038 ± 0.003	0.026 ± 0.002	0.046 ± 0.006	0.116 ± 0.003	0.027 ± 0.003	0.112 ± 0.005	0.062 ± 0.003
UO$_2$	–	b.d.l.	0.065 ± 0.010	0.092 ± 0.003	0.099 ± 0.008	0.115 ± 0.008	0.151 ± 0.006	0.232 ± 0.007	0.320 ± 0.016
Total	–	99.7 ± 0.4	99.4 ± 0.5	100.6 ± 0.2	100.4 ± 0.4	98.8 ± 0.4	100.7 ± 0.3	98.6 ± 0.5	99.5 ± 0.2
Trace elements (µg/g):		(n = 26)	(n = 3)	(n = 16)	(n = 24)	(n = 3)	(n = 28)	(n = 4)	(n = 13)
P	31	73.5 ± 15.6	22.6 ± 2.0	n.a.	n.a.	148 ± 11	82.9 ± 11.0	156 ± 7	n.a.
Ti	49	6.37 ± 2.46	4.11 ± 0.45	n.a.	n.a.	16.4 ± 0.6	8.16 ± 1.06	5.76 ± 0.38	n.a.
Y	89	440 ± 182	159 ± 4	n.a.	785 ± 55	618 ± 11	436 ± 3	1481 ± 35	n.a.
Nb	93	5.62 ± 3.97	10.2 ± 0.6	0.19 ± 0.06	1.61 ± 0.45	38.5 ± 4.0	8.03 ± 0.48	31.2 ± 1.0	n.a.
La	139	b.d.l.	0.021 ± 0.005	0.021 ± 0.005	0.021 ± 0.005	0.021 ± 0.005	0.021 ± 0.005	0.021 ± 0.005	n.a.
Ce	140	2.84 ± 1.89	113 ± 6	5.04 ± 0.34	16.9 ± 0.8	84.4 ± 4.8	14.3 ± 0.9	115 ± 6	n.a.
Pr	141	0.07 ± 0.05	0.206 ± 0.030	0.20 ± 0.07	0.18 ± 0.07	0.142 ± 0.004	0.057 ± 0.011	0.188 ± 0.011	n.a.
Nd	146	1.11 ± 0.83	2.63 ± 0.15	1.39 ± 0.45	1.95 ± 0.56	2.36 ± 0.06	1.14 ± 0.11	3.22 ± 0.14	n.a.
Sm	147	2.30 ± 1.45	2.60 ± 0.16	1.57 ± 0.26	3.95 ± 0.65	4.99 ± 0.34	1.90 ± 0.18	6.22 ± 0.34	n.a.
Eu	151	1.84 ± 1.10	0.499 ± 0.027	0.38 ± 0.10	0.39 ± 0.13	0.511 ± 0.037	0.061 ± 0.010	0.432 ± 0.037	n.a.
Gd	157	11.9 ± 6.7	5.94 ± 0.25	3.96 ± 1.04	15.6 ± 1.5	18.0 ± 0.5	8.96 ± 0.48	26.4 ± 0.7	n.a.
Tb	159	4.37 ± 2.37	n.a.	1.18 ± 0.11	5.55 ± 0.36	n.a.	3.27 ± 0.09	n.a.	n.a.
Dy	163	48.5 ± 23.7	13.5 ± 0.4	12.6 ± 0.8	67.1 ± 2.0	64.9 ± 0.4	37.5 ± 0.8	116 ± 3	n.a.
Ho	165	16.3 ± 7.2	3.17 ± 0.14	4.44 ± 0.26	25.7 ± 1.6	21.7 ± 0.6	13.1 ± 0.3	43.7 ± 1.1	n.a.
Er	166	63.6 ± 24.6	14.1 ± 0.8	19.5 ± 1.5	121 ± 9	92.8 ± 1.9	54.4 ± 1.0	207 ± 4	n.a.
Tm	169	12.1 ± 4.1	n.a.	4.51 ± 0.26	28.0 ± 2.1	n.a.	11.1 ± 0.2	n.a.	n.a.
Yb	173	104 ± 31	32.8 ± 1.5	45.0 ± 2.2	286 ± 19	217 ± 6	104.2 ± 4.2	537 ± 16	n.a.
Lu	175	16.6 ± 4.2	4.79 ± 0.18	7.20 ± 0.42	53.7 ± 1.8	30.6 ± 1.3	15.5 ± 0.9	81.7 ± 2.1	n.a.
Hf	178	5870 ± 270	16,550 ± 1300	10,610 ± 460	12,400 ± 500	12,690 ± 840	11,600 ± 240	14,420 ± 120	n.a.
Ta	181	n.a.	2.22 ± 0.29	n.a.	n.a.	20.4 ± 6.0	5.73 ± 0.38	9.22 ± 0.84	n.a.
Pb	204/204/207/208	b.d.l.	185 ± 19	83.2 ± 3.7	78.4 ± 4.2	380 ± 17	480 ± 32	690 ± 29	224 ± 8
Th	232	94.2 ± 94.9	312 ± 30	190 ± 20	413 ± 17	983 ± 29	240 ± 6	956 ± 43	585 ± 34
U	238	119 ± 68	541 ± 87	840 ± 20	923 ± 29	983 ± 68	1305 ± 57	1982 ± 58	2572 ± 96

Notes: Quoted uncertainties are 2σ. b.d.l. = not detected or mean below the respective EPMA or LA–ICP–MS detection limit. n.a. = not analysed.

[a] Major oxides for R–5 from Nasdala et al. (2018a) and trace elements from Zeug et al. (2018).

[b] Data for M257 from Nasdala et al. (2008).

[c] Data for M127 from Nasdala et al. (2016).

[d] Data for GZ8 from Nasdala et al. (2018b).

[e] Major-oxide EPMA data for G3 from Nasdala et al. (2004). Pb. Th and U concentrations for G3 from Kennedy (2000); determined by SIMS (secondary ion mass spectrometry) analysis using CZ3 (Pidgeon et al., 1994) as calibration material.
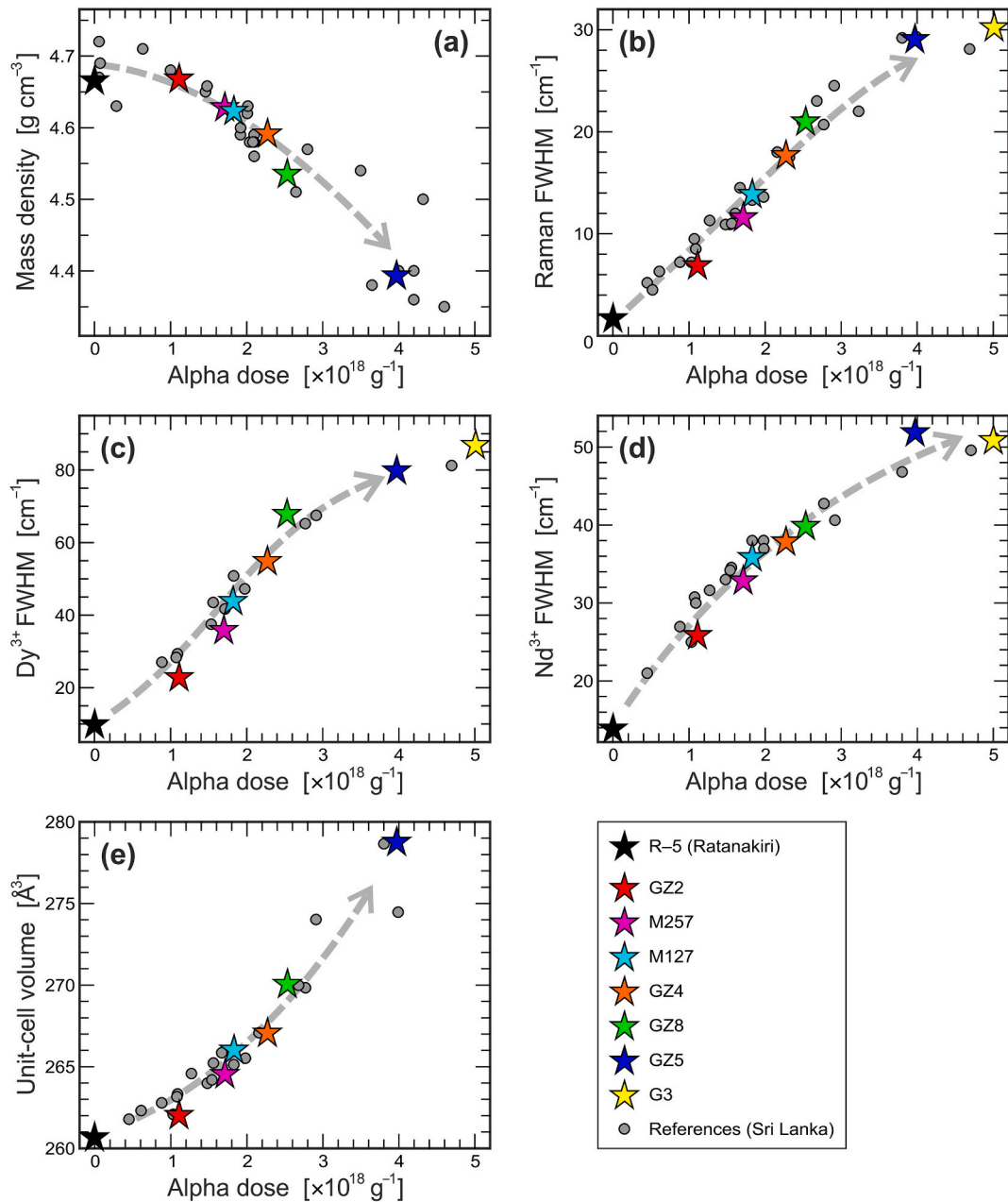
Fig. 3. Plots of (a) mass density, (b) FWHM of the ~1008 cm^{-1} Raman band, (c–d) FWHMs of the ~17,210 cm^{-1} ($^4F_{9/2} \rightarrow {}^6H_{13/2}$ transition of Dy^{3+}) and ~ 11,360 cm^{-1} ($^4F_{3/2} \rightarrow {}^4I_{9/2}$ transition of Nd^{3+}) PL lines, and (e) unit-cell volume, against the calculated alpha dose. Reference data for Sri Lankan zircon are shown as grey circles: mass densities from Vaz and Senftle (1971), Murakami et al. (1991), Ellsworth et al. (1994) and Zhang et al. (2000); Raman FWHMs and unit-cell volumes from Nasdala et al. (2004, 2018b); PL FWHMs from Lenz and Nasdala (2015) and Nasdala et al. (2018b). Grey arrows are visual guides and illustrate general "Sri Lankan trends" of parameter changes with increasing self-irradiation dose.

spectral trend increases appreciably with increasing radiation damage in the starting material. Only for the strongly radiation-damaged zircon GZ5, the apparent Raman shift – FWHM mismatch at moderate T_a results in data pairs that deviate considerably from data pairs defining progressive damage accumulation (Fig. 5). Shrinking of Raman FWHMs (Fig. 6) also depends on the degree of damage of the starting material. For GZ5 the FWHM decrease is moderate up to $T_a = 600$ °C, and more pronounced and more or less uniform at higher T_a. Moderately radiation damaged zircon, in contrast, shows an apparent three-step behaviour, with the strongest FWHM decreases in the T_a range 450–650 °C and

rather moderate decreases at higher T_a (Fig. 6).

Changes of FWHMs of Stark lines in PL spectra (Fig. S3) exhibit principally similar recovery trends, however, with much higher scatter and higher uncertainty of individual data. This is assigned to increasing uncertainties in data reduction (background correction, and deconvolution of lines that become broader and hence show more significant overlapping at elevated radiation damage; Fig. S2). Therefore, we focus on Raman spectroscopy in the present paper and provide PL FWHMs merely to facilitate comparison with published data.
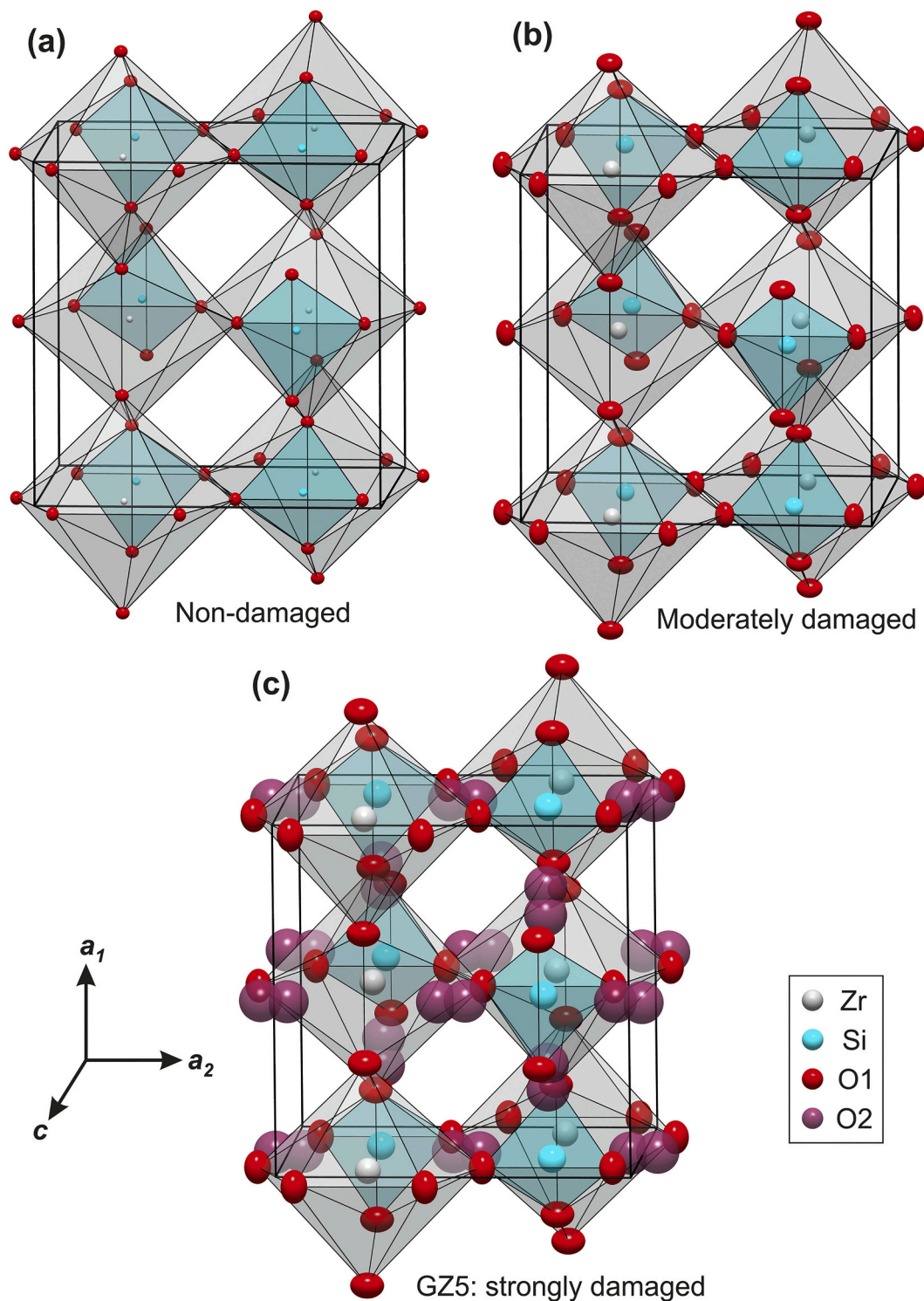
Fig. 4. Comparison of the structures of (a) virtually non-damaged zircon from Kragerø, Norway (data from Robinson et al., 1971) and (b) moderately radiation-damaged zircon from Sri Lanka (sample 269 of Ríos et al., 2000a) with (c) the severely radiation-damaged zircon GZ5 (present study). In the latter there are additional interstitial sites (purple ellipsoids; O2) that are occupied by oxygen ions to a limited extent (~4%). The anisotropic displacement ellipsoids for all atoms are drawn at the 80% probability level. (For interpretation of the references to colour in this figure legend, the reader is referred to the web version of this article.)
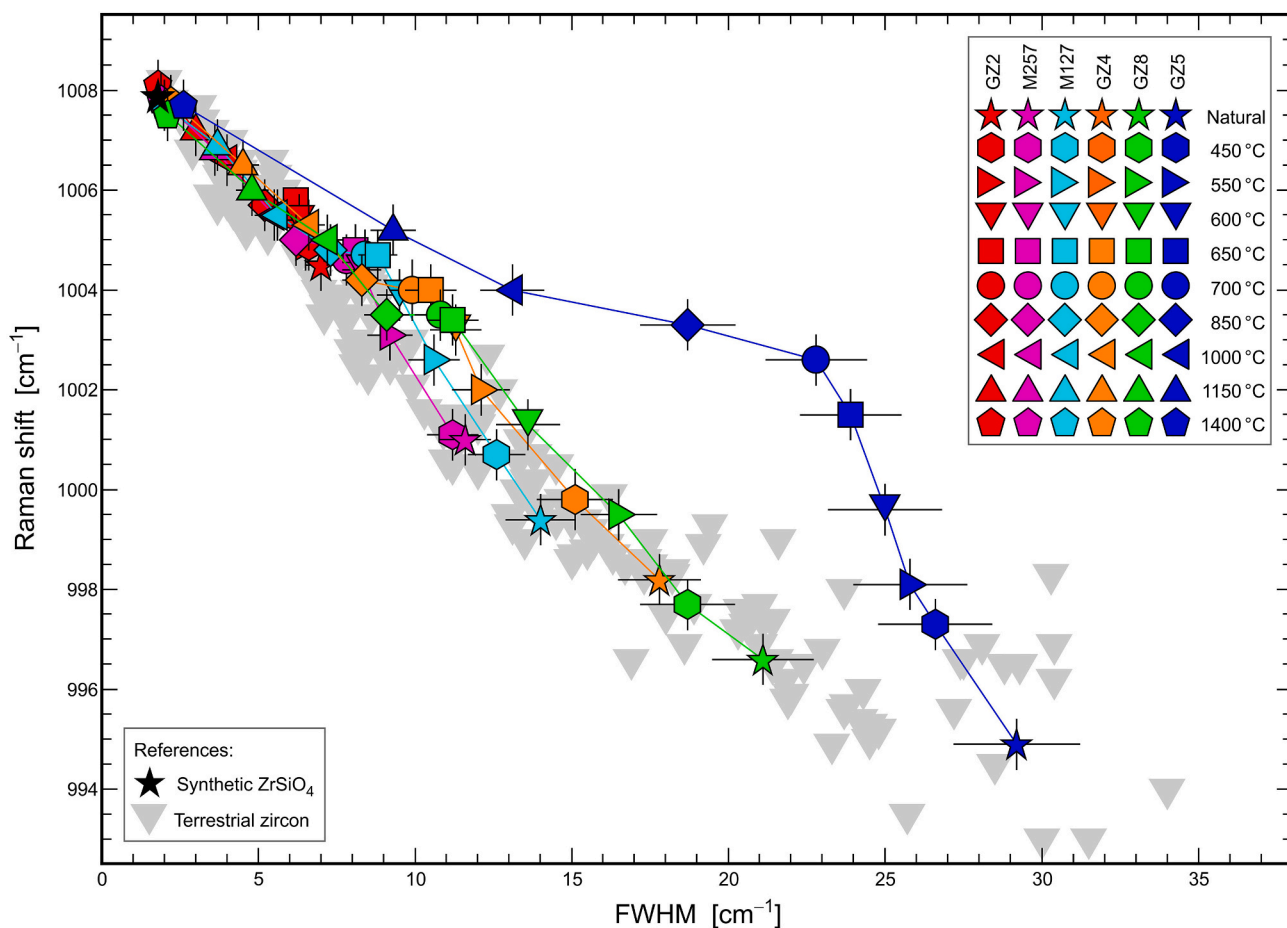
Fig. 5. Plot of spectral position versus broadening of the $\nu_3(SiO_4)$ Raman band. Compared to FWHM decreases, there are apparently over-proportional Raman-shift increases up to annealing temperatures of 650–700 °C. For the severely radiation-damaged zircon sample GZ5, the resulting spectral trend upon annealing deviates appreciably from the damage-accumulation trend (grey triangles). Reference parameters for terrestrial zircon extracted from Fig. 2 of Zhang et al. (2000), and from Nasdala et al. (2001, 2004, 2018b). Parameters for synthetic ZrSiO$_4$ were obtained from an un-doped crystal grown using a Li-Mo-flux technique (see Hanchar et al., 2001).
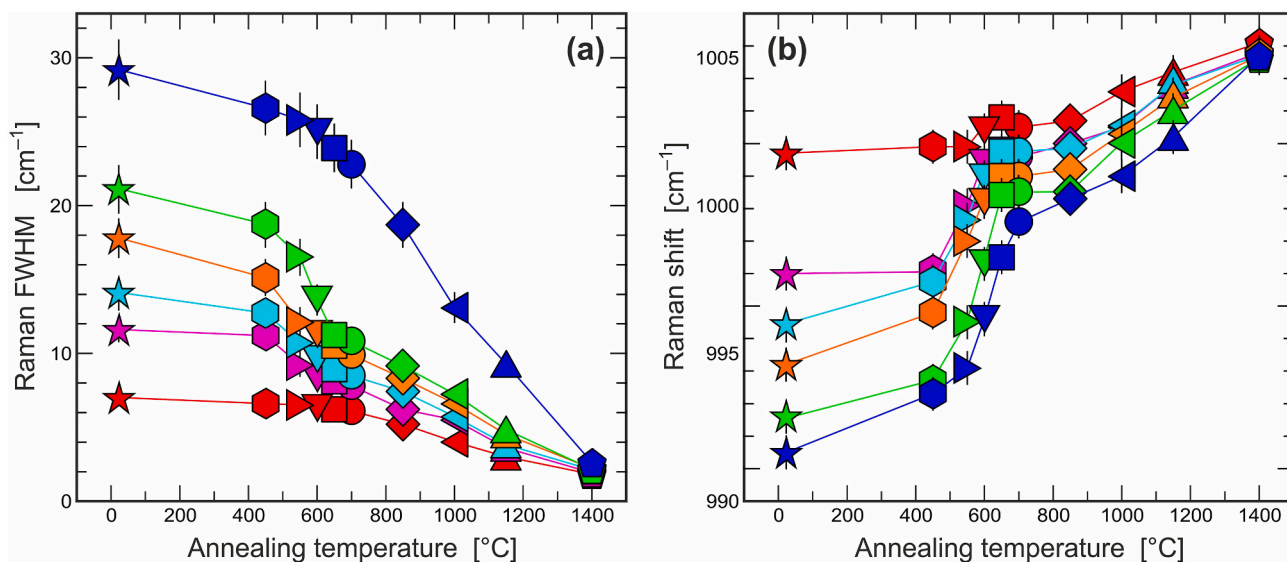
Fig. 6. Plot of (a) the width of the $\nu_3(SiO_4)$ Raman band and (b) its spectral position against annealing temperature. Symbols as in Fig. 5. Note that (in contrast to GZ2 and GZ5) moderately radiation-damaged zircon (M127, M257, GZ4, GZ8) has experienced particular FWHM decreases upon moderate annealing in the range T_a = 450–650 °C; most samples show particularly strong band upshift in this range.
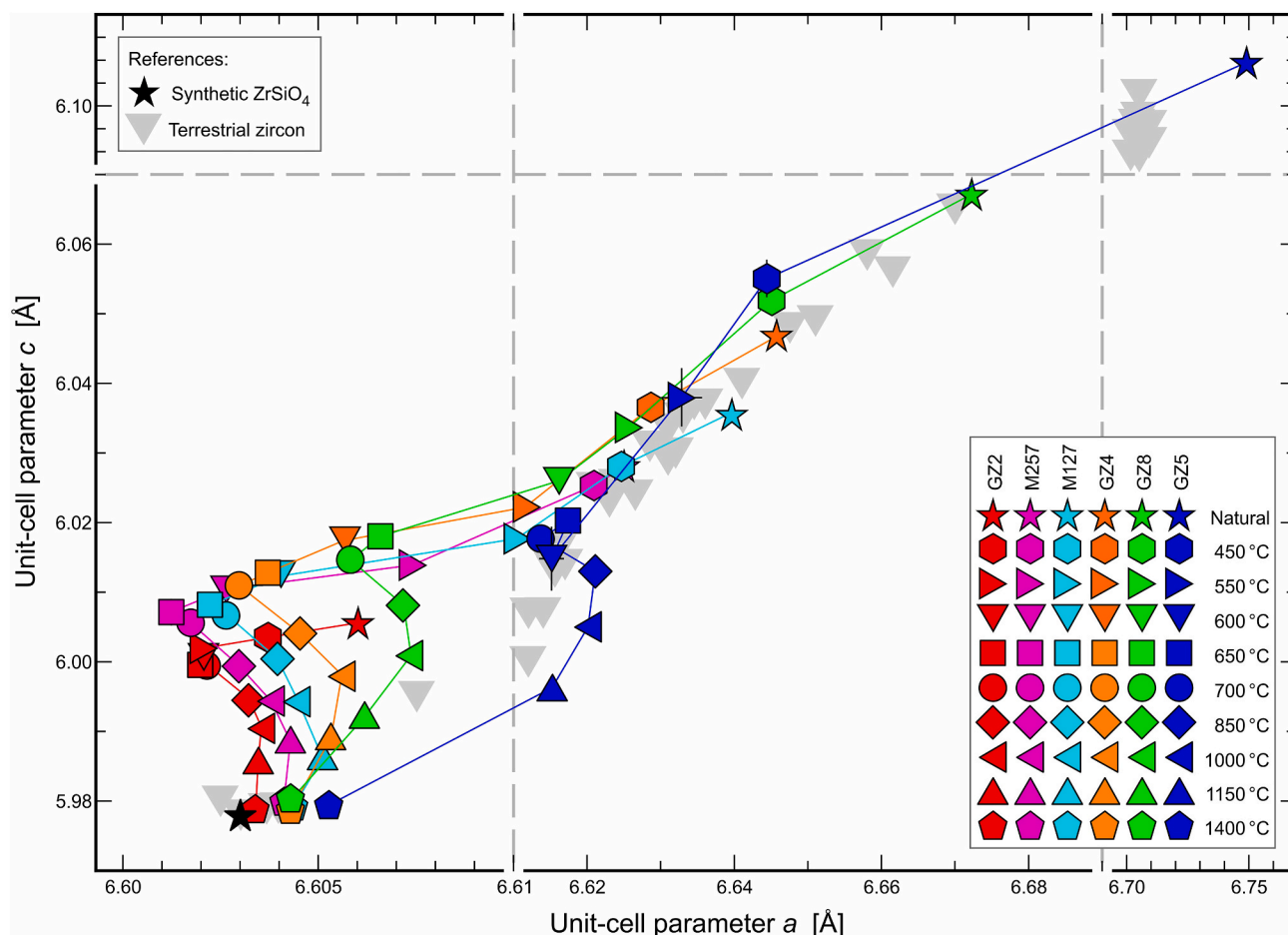
Fig. 7. Plot of unit-cell parameters c versus a. Note axis breaks with significant changes of scaling at $a = 6.61$ Å, $a = 6.69$ Å and $c = 6.07$ Å. Up to annealing temperatures of 650–700 °C, there is preferred a recovery (that for most samples results in high c/a ratios that deviate from the damage-accumulation trend; grey triangles). At higher annealing temperatures, there is preferred c recovery whereas a re-increases prior to final shrinking. Reference parameters for terrestrial zircon extracted from Fig. 4 of Holland and Gottfried (1955), and from Nasdala et al. (2004). Parameters for synthetic $ZrSiO_4$ from ICDD-PDF (International Centre for Diffraction Data, Powder Diffraction File) 6–266.

3.2.2. Single-crystal X-ray diffraction: Lattice parameters

A summary plot of unit-cell parameters c against a is provided in Fig. 7; individual plots for the six samples are contained in the ESM (Fig. S4). Unit-cell contraction depending on T_a is visualised in Fig. 8. Up to $T_a \sim 650$–700 °C, both of the two unit-cell parameters a and c change gradually, with preferred relaxation of a. Note that for the strongly radiation-damaged zircon GZ5, the extent of initial changes is particularly high, with about 73% (a) and 45% (c) of parameter recovery reached already at $T_a = 450$ °C (when compared to the entire change achieved at $T_a = 1400$ °C). For all samples – and thus independent from the initial degree of radiation damage – it was found that at $T_a \sim 700$ °C, unit-cell parameter a (~ 6.61 Å) apparently has recovered completely, compared to respective value at $T_a = 1400$ °C (Table S1; Fig. 7). This contrasts with unit-cell parameter c, whose reduction at $T_a = 700$ °C lies only between 28% (GZ2) and 70% (GZ5) compared to the full change at $T_a = 1400$ °C. At higher T_a (> 650–700 °C), unit-cell parameter c continues to contract gradually, to the final value of ~ 5.98 Å, whereas unit-cell parameter a shows a notable re-increase at $T_a = 850$–1150 °C, before decreasing again to the final value of 6.603–6.605 Å at $T_a = 1400$ °C. It seems worthy of note that for the mildly to moderately radiation-damaged samples GZ2 to GZ4, the value of unit-cell parameter a is notably lower at $T_a = 700$ °C, compared to $T_a = 1400$ °C, whereas the more radiation-damaged samples GZ5 and GZ8 yielded the lowest a value at $T_a = 1400$ °C (Fig. 7; Table S1; Fig. S4).
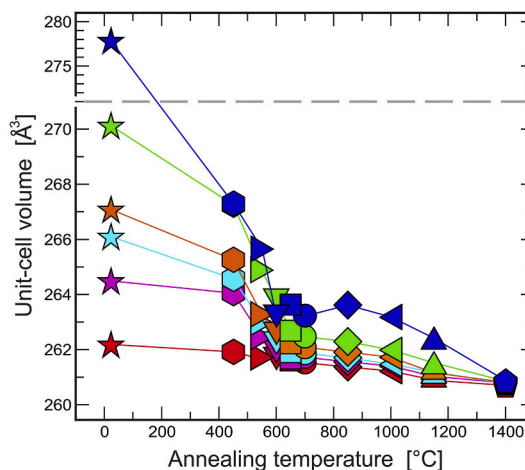

Fig. 8. Plot of unit-cell volume versus annealing temperature. Note y-axis break with significant change of scaling at $V = 271$ Å³. Symbols as in Fig. 7. Low- to moderate-T annealing ($T_a \leq 650$ °C) is characterised by distinct cell-volume shrinking.
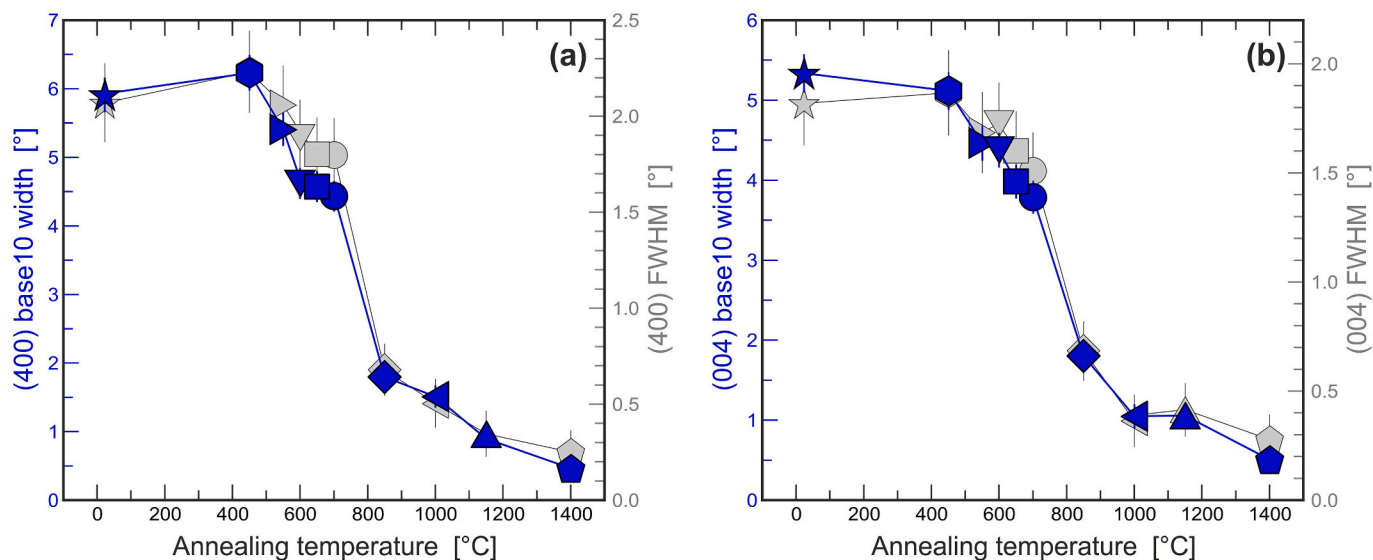
Fig. 9. Plot of the widths of rocking curves of selected Bragg reflections [(a) (400); (b) (004)] of zircon GZ5 against annealing temperature. Base10 width = measured at the 10%-level of the peak height (blue symbols; left ordinate axes). FWHM = measured at the 50%-level of the peak height (grey symbols; right ordinate axes). (For interpretation of the references to colour in this figure legend, the reader is referred to the web version of this article.)
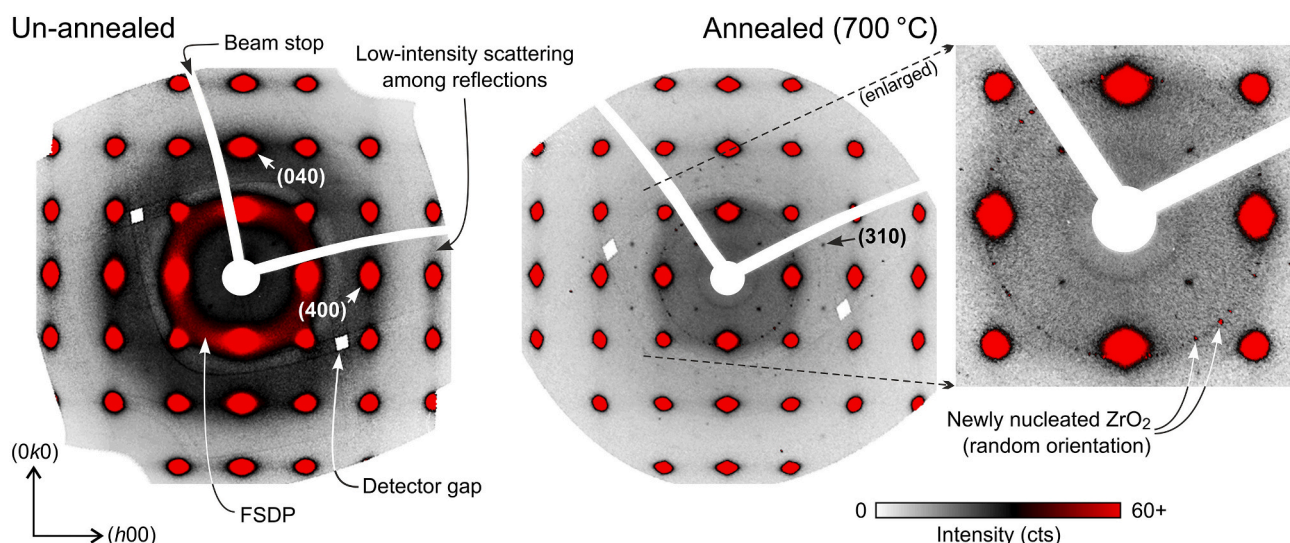

Fig. 10. Reciprocal space maps in the (*hk*0) plane, shown for the examples of the un-annealed sample GZ5 and its partially annealed (700 °C; 96 h) counterpart. White areas are artefacts (two detector gaps and beam-stop areas). In the map of the un-annealed sample, a red ring represents the FSDP (first sharp diffraction peak) of the "X-ray-amorphous" ZrSiO$_4$ fraction. Diffuse scattering among diffraction peaks of zircon is visible as faint grey areas. Its intensity is much lower than that of the diffuse scattering in close proximity around the Bragg peaks (round to oval, red areas). In the map of the partially annealed sample, the FSDP has disappeared. Instead, there are small sharp (101) or (011) reflections of newly nucleated tetragonal ZrO$_2$ with random crystallographic orientation. Note that the sharp Bragg peaks themselves (intensities on the order of 10^4–10^5 cts), located in the centres of the big, round to oval red areas, are not seen individually in the maps. This is because to the colour-coding (limited to the range 0–60 cts) that was chosen to visualise low-intensity phenomena. (For interpretation of the references to colour in this figure legend, the reader is referred to the web version of this article.)

For all samples except the strongly radiation-damaged zircon GZ5, the different annealing regimes of unit-cell parameters *a* and *c* result at intermediate annealing temperatures ($T_a = 600$–1000 °C) in *c/a* ratios that deviate from those of progressively radiation-damaged zircon (Fig. 7). This is consistent with earlier observations of obvious *c/a* mismatches resulting from preferred *a* recovery upon partial annealing (Weber, 1990), which was discussed as possible means for unravelling temperature treatment for colour enhancement of *gem* zircon (Nasdala et al., 2004). For all samples except the mildly damaged zircon GZ2 it was found that the vast majority of unit-cell contraction occurs already

during moderate annealing with $T_a \leq 650$ °C (Fig. 8; Table S1).

3.2.3. Single-crystal X-ray diffraction: Peak widths and diffuse scattering

It is known that, in contrast to X-ray powder diffraction, 3D resolution functions of X-ray single-crystal experiments exhibit a complicated and anisotropic behaviour that depends on the reciprocal space position. Proper correction of resolution effects is only possible in relatively simple cases (Welberry and Weber, 2016). Even shape and size of the specimen analysed have perceptible influence on the diffuse scattering. Therefore, experimental minimisation of resolution effects is essential.

In spite of "fine slicing" of diffraction patterns (frames were taken every 0.125° of ω rotation), our experimental setting was certainly suboptimal, and our results cannot compete with the excellent quality achieved for two weakly radiation-damaged zircon samples analysed by Ríos and Salje (1999). Nevertheless, broad diffuse scattering around Bragg peaks was clearly observed for all three un-annealed samples analysed, being strongest for GZ5, moderate for GZ4, and low (but still noticeably different from the annealed counterpart) for GZ2 (Fig. S5).

Plots of widths of the (400) and (004) Bragg peaks of zircon GZ5 are presented in Fig. 9. These values (FWHM and base10 width) were obtained from rocking curves (Fig. S6), which in turn are plots of the integral intensity of frames (i.e., two-dimensional diffraction patterns, Fig. S5) against the rotation angle ω. The trends observed are essentially identical, with base10 widths (that are obviously more sensitive than FWHMs to low-intensity, diffuse scattering) being affected by lower relative uncertainties. Widths of Bragg peaks do not show significant changes after annealing at $T_a = 450\,°C$. At intermediate T_a [450–850 °C for (400) and 450–1000 °C for (004)] they narrow appreciably, with the maximum change between $T_a = 700\,°C$ and $T_a = 850\,°C$. Further narrowing at even higher T_a is comparably minor. While particle size and strain effects can increase all peak dimensions in a similar manner, the peak width along rocking angle ω that is used here is mainly influenced by mosaic spread, which indicates twisting of various parts of the crystal against each other (Salje et al., 1999).

Reciprocal space maps reconstructed from 360° Φ scans for the un-annealed sample GZ5 and its partially annealed ($T_a = 700\,°C$) counterpart are presented in Fig. 10. The map of the un-annealed sample shows several peculiarities that support the assignment of this sample as strongly radiation damaged. Apart from the "regular" diffuse scattering in proximity of the main Bragg peaks, there is lowest-intensity diffuse scattering between neighbouring Bragg peaks (light grey areas in the left part of Fig. 10). The latter phenomenon has, to the best of our knowledge, never been described before. Further, a ring-like phenomenon is seen near ~13.7° 2θ, located near the positions of the strongest diffraction peaks of zircon [(200), (020), ($\bar{2}$00) and (0$\bar{2}$0)]. This ring represents the FSDP (first sharp diffraction peak) of the sample's (X-ray) amorphous volume fraction. It is followed by a second diffraction ring (dark grey) with maximum intensity near ~24.1° 2θ. Further Φ scans were done, and reciprocal space maps were reconstructed, for the two GZ5 chips annealed at $T_a = 550\,°C$ (not shown) and $T_a = 700\,°C$ (Fig. 10). At $T_a = 550\,°C$, the map still resembles that of the un-annealed sample, with the intensity of the FSDP having somewhat decreased. Low-intensity Bragg peaks of zircon [such as (310)] have become obvious, which points to lowered peak widths and thus intensity gain per detector pixel. At $T_a = 700\,°C$ the reciprocal space map shows significant changes. Any evidence of the (X-ray) amorphous volume fraction is gone. Instead, there are several small new diffraction peaks, which are assigned to the (101) and (011) reflections of newly formed, randomly oriented tetragonal ZrO_2. Whether or not lowest-intensity diffuse scattering between adjacent diffraction peaks is still present, cannot be evaluated as intensity differences to the background are marginal.

3.2.4. Single-crystal X-ray diffraction: Structure refinement of zircon GZ5

For all nine T_a in the range 450–1400 °C, refinements of the occupancy of the O-interstitial site near Wyckoff position 8d were made. Results are shown in Fig. 11. It seems that the occupancy of the O-interstitial site is significant only up to $T_a = 550\,°C$, whereas at $T_a \geq 600\,°C$, only 1% (or even less) of all O atoms are at interstitial sites.
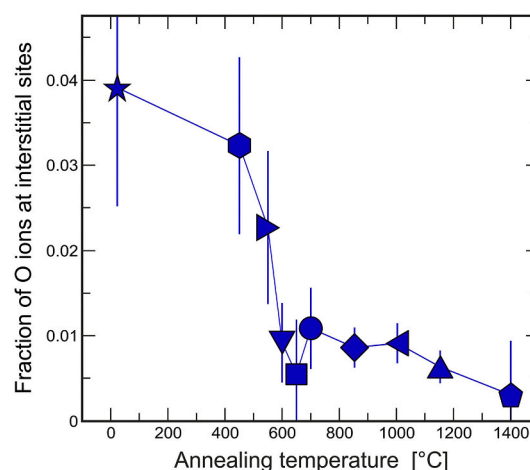

Fig. 11. Decrease of the occupation of O-interstitial sites in the lattice of sample GZ5 with increasing T_a.

4. Discussion

4.1. Generalities

The six *gem*-zircon samples (GZ2, GZ4, GZ5, GZ8, M127 and M257) have Late Neoproterozoic (Ediacaran) to Early Cambrian (Terreneuvian) U–Pb ages of 561–524 Ma (Table 1), which correspond well to previous age results reported for zircon from gem placers in the Ratnapura district (Holland and Gottfried, 1955; Kröner et al., 1987; Nasdala et al., 2004). These ages are assigned to either granites and granitic pegmatites (Chakoumakos et al., 1987; Kröner et al., 1987) or collisional metamorphism (Santosh et al., 2014). The latter is supported by some very high $\delta^{18}O$ values [> 13‰ VSMOW (Vienna Standard Mean Ocean Water)] that are untypical of igneous zircon and rather point to metasomatic origin (Cavosie et al., 2011; Nasdala et al., 2008). Also, (U–Th)/ He ages of 480–419 Ma (Table 1; detailed data are presented in Table S2) are consistent with previously published (U–Th)/He ages for unheated Sri Lankan gem zircon (Ginster et al., 2019; Hurley, 1954; Nasdala et al., 2004, 2018b). These "regular" (U–Th)/He ages allow us to exclude any heat-treatment of samples prior to our study.

Observed parameter changes (corresponding to calculated alpha doses; see again Fig. 3) characterise GZ5 and G3 as the most severely radiation-damaged samples. Sample GZ4, in contrast, is only moderately radiation-damaged, in spite of its fairly high Th content (Table 2). The more "damaging" nature of U is explained by the more than three times shorter radioactive half-life of the dominant isotope ^{238}U, compared to that of ^{232}Th.

It is important to note that widths of spectroscopic signals and unit-cell constants of samples annealed at $T_a = 1400\,°C$ (Table 1) are widely similar to those of the virtually non-radiation-damaged zircon sample R–5 (Zeug et al., 2018) and synthetic $ZrSiO_4$ (Nasdala et al., 2002). This implies first that structural recovery of the initially present, accumulated radiation damage through 96-h annealing at 1400 °C is nearly complete. Second, deviations of parameters of the un-annealed samples from that of synthetic un-doped $ZrSiO_4$ are principally caused by the accumulated self-irradiation damage, whereas potential effects of chemical variations (i.e. parameter variations caused by the presence of non-formula chemical constituents) are almost negligible.

It has been proposed that in the case of minerals that have suffered high alpha-decay doses, the formation and emplacement of the

radiogenic He (i.e. alpha particles) may contribute to macroscopic swelling (Weber et al., 1998) and even to unit-cell expansion (Seydoux-Guillaume et al., 2002). Such potential effects of He on zircon can be excluded for our samples, based on a simple volume-balance calculation. Since the closure of the (U–Th)/He system ~446 Myr ago, zircon GZ5 has experienced ~3.32 × 10^{18} α-decay events per g. Based on the sample's mass density of ~4.395 g/cm^3, the above dose corresponds to a concentration of ~1.46 × 10^{19} He/cm^{-3}. Considering the unit-cell volume of ~279 Å^3 (or ~ 2.79 × 10^{-22} cm^3), there is an average of 0.004 He atoms per unit cell, which is insignificant. In conclusion, trapping of the radiogenic He (and also its subsequent escape upon heat treatment) can have only very minor contribution – if detectable at all – to the expansion (and subsequent contraction) of the unit-cell volume.

4.2. Structure of un-annealed zircon GZ5

In discussing refinement results, it needs to be considered that structural parameters obtained by single-crystal X-ray diffraction analysis do not represent the entire sample, but are related to (the mean of) its remnant crystalline fraction. This crystalline fraction of sample GZ5 shows extensive but nearly isotropic unit-cell swelling, compared to undamaged zircon (Robinson et al., 1971). Unit-cell parameter a of zircon GZ5 is lengthened by $\Delta a/a = 2.15 \pm 0.05\%$, and unit-cell parameter c by $\Delta c/c = 2.28 \pm 0.07\%$. Consequently, the highly anisotropic expansion behaviour of moderately radiation-damaged zircon (for instance, $\Delta a/a = 0.17 \pm 0.05\%$ against $\Delta c/c = 0.67 \pm 0.05\%$ based on data of by Ríos et al., 2000a; compare also zircon GZ4 studied herein; Table 1) is not observed anymore at more elevated damage-accumulation stages.

The bisdisphenoidal polyhedron [or dodecadeltahedron, often referred to as (triangular) dodecahedron] around the central Zr^{4+} of the ZrO_8 unit can be considered as two inter-penetrating ZrO_4 tetrahedrons. One of these tetrahedrons is elongated along c, while the other one is compressed in the ab plane. This results in four longer, symmetric Zr–O distances with 2.3226(15) Å, and four shorter Zr–O distances with 2.1755(16) Å. Analogous to unit-cell dimensions, these Zr–O distances of GZ5 represent strong but barely anisotropic expansion compared to un-damaged zircon (compressed tetrahedron +2.09 ± 0.08%; elongated tetrahedron +2.41 ± 0.07%; CZ5 relative to data of Robinson et al., 1971; Fig. S1) whereas moderately radiation-damaged zircon (compressed tetrahedron +0.07 ± 0.06%; elongated tetrahedron +0.60 ± 0.06%; sample 269 of Ríos et al., 2000a, relative to data of Robinson et al., 1971) shows moderate but strongly anisotropic expansion.

After fitting all atoms including anisotropic displacement parameters (ADPs) and extinction and weighting parameters, the subsequently calculated difference Fourier map showed weak residual peaks. These residuals correspond roughly to Wyckoff position 8d [for example (¼, ¼, ¼); a position that is normally unoccupied in the zircon structure]. In Fig. 4c, these positions correspond to the centres of purple dumbbells. For simple statistical reasons (66.7% of all atoms present are oxygen), and because the displacement energy of O is lower than that of Zr and Si (Moreira et al., 2009, 2010), results of Monte Carlo simulations (Nasdala et al., 2018a) predict that the vast majority of displaced lattice atoms in radiation-damaged zircon will be oxygen. Therefore it appears more than reasonable to assume that the normally unoccupied interstitial position is occupied by oxygen. These oxygen interstitials seem to represent an alternative rotation of SiO_4 tetrahedrons. However, the assumption that the ideal Wyckoff position 8d was occupied (i.e., if the dumbbells in Fig. 4c were spheres) would result in a unrealistic Si–O distance of 1.853 ± 0.002 Å. This and the obtained displacement parameters suggest that the interstitial does not correspond to the highly symmetric Wyckoff position 8d but a lower-symmetry position nearby. Much more reasonable results were obtained by constraining only the y value. The position is proposed as (0.288, ¼, 0.240), resulting in a reasonable Si–O distance of 1.60 ± 0.07 Å. The level of occupation of the interstitial site is fairly low; our results suggest that about 96% of all

oxygen atoms are at the "regular" O1 sites, and only about 4% at the interstitial O2 sites.

4.3. Thermal annealing of radiation damage

Structural recovery of radiation-damaged zircon upon dry heat treatment is a non-uniform process whose sequence depends strongly on (i) the initial degree of accumulated radiation damage, (ii) the analysis technique applied and (iii) the actual physical parameter used for evaluation. Most of the parameter changes with increasing T_a observed herein seem to exhibit a two- or three- or even more-step behaviour. To simplify and straighten the discussion, we focus on substantial differences between low-T and high-T annealing.

Low-T annealing ($T_a \leq 650$–700 °C) is characterised by preferred recovery of Raman shifts (compared to Raman FWHMs; Fig. 5), preferred shrinking of unit-cell dimension a (compared to c; Fig. 7) and extensive contraction of the unit-cell volume (Fig. 8), rather moderate narrowing of widths of rocking curves (Fig. 9), virtually complete recrystallization of the amorphous volume fraction (Fig. 10), and significant reduction of the occupation of O-interstitial sites (Fig. 11). Within the low-T annealing step, changes at $T_a = 450$ °C seem to be rather moderate, compared to parameter-versus-T_a trends in the T_a range 450–700 °C (Figs. 6, 8, 9, 11), with the only exception of strong unit-cell shrinking of sample GZ5 (Fig. 8). Low-T annealing is driven by epitaxial growth of the crystalline volume fraction at the expense of the amorphous volume fraction and the recovery of low-energy defects (preferentially related to O interstitials; Crocombette, 1999), resulting in significant reduction of strain and in increase of the mean size of coherently scattering domains. Our observation of (in the present case, subordinate) ZrO_2 formation instead of formation of crystalline $ZrSiO_4$ in the amorphous phase is consistent with earlier findings (Capitani et al., 2000; Nasdala et al., 2002). Ellsworth et al. (1994) discussed that in glassy $ZrSiO_4$, nucleation of tetragonal ZrO_2 (and with that, phase decomposition into tetragonal ZrO_2 and glassy SiO_2) is energetically favoured.

Due to the resolution limitations (e.g. divergent beam) and the nature of our strongly radiation-damaged zircon sample, the observed broad diffuse scattering around the Bragg peaks is mostly due to particle-size broadening. Our results cannot be compared directly with results of Ríos and Salje (1999) who observed Huang-type diffuse scattering on moderately radiation-damaged zircon. Huang scattering is diffuse scattering originating from relaxations due to point defects (Welberry and Weber, 2016). Salje et al. (1999) observed that the ω broadening of moderately damaged zircon does exceed only slightly the spread in the diffraction angle. This observation supports the interpretation that the diffuse scattering observed for GZ5 is dominated by "particle size" effects rather than by heterogeneous strain fields. In the interpretation it needs to be considered that the diffuse-scattering contribution of interstitials is more extensive than that of vacancies (Dederichs, 1973), that is, even though a Frenkel defect consist of interstitial and vacancy, mainly effects of interstitials are observed. As the diffuse scattering around main Bragg peaks is mainly due to the small sizes of coherently scattering domains (often called particle sizes), its intensity loss (Fig. 10) is assigned predominantly to epitaxial growth of the crystalline volume fraction at the expense of the amorphous fraction. In contrast, random nucleation in the X-ray amorphous phase is considered subordinate. This is because Sri Lankan zircon with a calculated self-irradiation dose of ~4 × 10^{18} α/g has a significant amorphous fraction (about 27% according to Weber, 1990, and about 63% according to Ríos et al., 2000b, respectively). If the apparent disappearance of the FSDP at $T_a = 700$ °C was related to random nucleation in the amorphous phase, reflections of newly formed crystals should make a significant contribution to the reciprocal space map, which however is not observed (Fig. 10).

Similar to observations by Salje et al. (1999), random orientations or broad angular distributions of crystalline islands do not seem to exist in

our un-annealed samples. In contrast, the annealed sample GZ5 has yielded additional diffraction spots that are assigned to newly nucleated domains of random orientation (Fig. 10). The reciprocal space maps obtained herein show that both nucleation and growth of crystalline domains within the amorphous volume fraction, and the disappearance of the latter, occur at $T_a \leq 700$ °C.

Higher-T annealing ($T_a \geq 700$ °C) results in preferred recovery of Raman FWHMs (compared to Raman shifts; Fig. 5), mild unit-cell contraction (Fig. 8) and significant narrowing of rocking curves (Fig. 9). Here, it is most remarkable that unit-cell dimension a re-increases ($T_a = 750$–1150 °C) prior to final shrinking ($T_a = 1000$–1400 °C; Figs. 7 and S3). This is explained as a side-effect of healing of defects along the c axis, leading to the formation of new bonds among neighbouring ZrO$_8$ and SiO$_4$ polyhedrons. As long as the initial bonds are damaged, Zr ↔ Si repulsion (Tokuda et al., 2019) affects unit-cell elongation along the c axis parameter and therewith slight compression of the a axes due to further ZrO$_8$ polyhedron deformation, which both recovers at T_a 750–1150 °C.

The apparently incongruent annealing behaviour of radiation-damage-expanded unit-cell parameters a and c was observed in several annealing studies already (e.g. Colombo et al., 1999; Nasdala et al., 2004; Weber, 1990). A differing, weaker trend of incongruent a and c expansion was detected for progressively radiation-damaged zircon (Holland and Gottfried, 1955; Murakami et al., 1991; Nasdala et al., 2004). The preferential relaxation of the a axis expansion was interpreted by Ríos et al. (2000a) by the consideration that for weakly damaged zircon, radiation damage seems to have more important effects on Zr and O than on Si ions. Consequently, interstitial-vacancy pairs related to the large ZrO$_8$ polyhedrons (that are the least stable structural unit in zircon; Mursic et al., 1992; Ríos et al., 2000a) are created at initial damage-accumulation stages. In contrast, Si atoms are expected to be well confined inside rigid SiO$_4$ tetrahedrons. For the completely annealed sample GZ5 ($T_a = 1400$ °C), the Zr–O bonds to O atoms in a shared SiO$_4$ tetrahedron edge are ~0.147 Å longer (GZ5; $T_a = 1400$ °C) than those to O atoms not involved in edge-sharing with the tetrahedron (Robinson et al., 1971, found a difference of ~0.137 Å for virtually un-damaged zircon; cf. Fig. S1). Furthermore, the O–Si–O angle to this shared edge is only 97.09(3)° compared to 116.00(3)° at the other tetrahedron edges (Robinson et al., 1971, found 97.0° and 116.1°, respectively; cf. Fig. S1). Both structural features are indications for a strong repulsive interaction between the neighbouring Zr and Si atoms along the c axis (e.g. Kolesov et al., 2001; Robinson et al., 1971; Tokuda et al., 2019). At high pressure, this makes the c direction more than twice as stiff as the perpendicular a directions (e.g. Binvignat et al., 2018; Hazen and Finger, 1979). As the structure of zircon is softer along the a axes, tilting of polyhedrons around the corner-sharing links along these axes requires less energy (Ríos et al., 2000a). In contrast, annealing defects produced by expansion along the c axis is more difficult, and hence requires higher T_a, because of the strong repulsion of Zr and Si atoms.

The FWHMs of the rocking curves of angle ω (Fig. 9) are mostly related to the angular distribution of lattice planes (*hkl*) of crystalline domains called mosaic spread (Salje et al., 1999). This twisting of crystalline domains is in turn generated, or at least enhanced, by local swelling of their neighbouring defect-rich, aperiodic regions (Salje et al., 1999). Therefore, at annealing, we assume to see mainly the reduction of lattice twisting first by the shrinkage of the amorphous volume fraction, which reduces the local swelling, and then at higher temperatures ($T_a > 700$ °C) by volume increase of crystalline domains due to defect recovery (Pruneda et al., 2004). The onset of FWHM decrease in rocking curves only at $T_a > 450$ °C might be assigned to a "reversal" of the damage-accumulation process, where at elevated stages no further broadening is observed (Salje et al., 1999).

5. Conclusions

Present single-crystal results, obtained using two different X-ray systems, allow us to verify for the first time that low-T annealing ($T_a \leq 700$ °C) of strongly radiation-damaged zircon – whose degree of damage is assigned in between the first and second percolation points (Salje et al., 1999) – involves nearly complete recrystallization of the amorphous volume fraction. This is indicated by the disappearance of the FSDP and intensity decreases of diffuse scattering around the Bragg peaks.

Our results suggest that the question may be inept whether dry annealing of partly radiation-damaged zircon is a two-step or three-step or even more-step process? Potential answers scatter and seem to depend on the initial degree of damage and the technique and parameter used for evaluation. Most of our results, however, indicate two different regimes at $T_a \leq 700$ °C and above. The first step is characterised by epitaxial growth of the crystalline volume fraction at the expense of the aperiodic volume fraction, along with significant decrease of O occupation at interstitial sites and unit-cell contraction. In addition, there appear tiny amounts of newly nucleated tetragonal ZrO$_2$. In the crystalline volume fraction, only low-energy defects are healed up to $T_a \leq 700$ °C, resulting in significant unit-cell shrinking along the a axis and with that, in major unit-cell compaction. Decreasing bond lengths cause increased Raman-shift values. Healing high-energy defects at high T_a (~ 700–1400 °C) mainly lowers unit-cell parameter c. The accompanying, remarkable re-increase of unit-cell parameter a ($T_a = 750$–1150 °C; hitherto not described) prior to final ($T_a = 1400$ °C) shortening is assigned to recovery of contorted ZrO$_8$ polyhedrons. The overall improvement of the short-range order results in narrowing of the Raman FWHM.

For a particular heat-treatment experiment, the exact "degree of recovery" within the (at least) two-step annealing process is difficult to define and quantify. Many of the analyses done herein (obtaining rocking curves of Bragg peaks, structural refinement, reciprocal space maps) are time-consuming and connected with enormous effort; their routine use is hence impractical. Also, conventional X-ray diffraction is not a micrometre-scale technique and its application will fail in studying zoned samples. In routine annealing studies, the quick and undemanding micro-Raman technique will therefore remain to be the preferred method of choice for monitoring structural recovery of zircon. In spite of still existing controversies on how to interpret variations of Raman parameters, our results may help analysts to correlate observed changes in Raman spectra to certain structural recovery processes.

Even though we were able to achieve significant progress in our understanding of thermal recovery processes of radiation-damaged zircon, our findings alone are insufficient to explain the effectiveness of the CA–TIMS technique, that is, why thermal treatment often leads to improved U–Pb results? We found that above 700 °C, initially amorphous volume fractions are turned into a ZrSiO$_4$ – tetragonal ZrO$_2$ composite. Due to its tiny volume fraction, ZrO$_2$ is considered insignificant for bulk properties. On the other hand, it may be speculated that such composite is less robust to HF etching, compared to single-crystal zircon. If confirmed to be true, this would explain the preferred removal of initially more radiation-damaged material during CA–TIMS pre-treatment. Further studies involving HF etching before and after annealing are necessary to address this hypothesis. In the present work, the recovery of concordant zircon was studied whereas full understanding of CA–TIMS will require the conduction of experiments that also include samples having disturbed U–Pb systems, to finally assign certain degrees of structural recovery to certain changes in U–Pb discordance.

Declaration of Competing Interest

The authors declare that they have no known competing financial interests or personal relationships that could have appeared to influence

the work reported in this paper.

Acknowledgements

Appendix A. Supplementary data

Supplementary data to this article can be found online at https://doi.org/10.1016/j.lithos.2021.106523.

References

Binvignat, F.A.P., Malcherek, T., Angel, R.J., Paulmann, C., Schlüter, J., Mihailova, B., 2018. Radiation-damaged zircon under high pressures. Phys. Chem. Miner. 45, 981–993.

Capitani, G.C., Leroux, H., Doukhan, J.C., Ríos, S., Zhang, M., Salje, E.K.H., 2000. A TEM investigation of natural metamict zircons: structure and recovery of amorphous domains. Phys. Chem. Miner. 27, 545–556.

Cavosie, A.J., Valley, J.W., Kita, N.T., Spicuzza, M.J., Ushikubo, T., Wilde, S.A., 2011. The origin of high $\delta^{18}O$ zircons: marbles, megacrysts, and metamorphism. Contrib. Mineral. Petrol. 162, 961–974.

Chakoumakos, B.C., Murakami, T., Lumpkin, G.R., Ewing, R.C., 1987. Alpha-decay-induced fracturing in zircon: the transition from the crystalline to the metamict state. Science 236, 1556–1559.

Cherniak, D.J., Watson, E.B., 2001. Pb diffusion in zircon. Chem. Geol. 172, 5–24.

Colombo, M., Chrosch, J., Salje, E.K.H., 1999. Annealing metamict zircon: a powder X-ray diffraction study of a highly defective phase. J. Am. Ceram. Soc. 82, 2711–2716.

Corfu, F., 2009. When the CA–TIMS therapy fails: the over-enthusiastic, the mixed up, and the stubborn zircon. EOS T. Am. Geophys. Un. 90 (52). Fall Meeting Suppl, abstr. V53B–05.

Corfu, F., 2013. A century of U-Pb geochronology: the long quest towards concordance. Geol. Soc. Am. Bull. 125, 33–47.

Crocombette, J.-P., 1999. Theoretical study of point defects in crystalline zircon. Phys. Chem. Miner. 27, 138–143.

Crocombette, J.-P., Ghaleb, D., 2001. Molecular dynamics modeling of irradiation damage in pure and uranium-doped zircon. J. Nucl. Mater. 295, 167–178.

Davis, D.W., Williams, I.S., Krogh, T.E., 2003. Historical development of zircon geochronology. In: Hanchar, J.M., Hoskin, P.W.O. (Eds.), Zircon. Reviews in Mineralogy and Geochemistry, vol. 53. Miner. Soc. Am., Washington, DC, pp. 145–181.

Dederichs, P.H., 1973. The theory of diffuse X-ray scattering and its application to the study of point defects and their clusters. J. Phys. F: Met. Phys. 3, 471–496.

Devanathan, R., Corrales, L.R., Weber, W.J., Chartier, A., Meis, C., 2006. Molecular dynamics simulation of energetic uranium recoil damage in zircon. Mol. Simul. 32, 1069–1077.

Ellsworth, S., Navrotsky, A., Ewing, R.C., 1994. Energetics of radiation damage in natural zircon ($ZrSiO_4$). Phys. Chem. Miner. 21, 140–149.

Ende, M., Kirkkala, T., Loitzenbauer, M., Talla, D., Wildner, M., Miletich, R., 2020. High-pressure behavior of nickel sulfate monohydrate: Isothermal compressibility, structural polymorphism, and transition pathway. Inorg. Chem. 59, 6255–6266.

Ewing, R.C., 1994. The metamict state: 1993 - the centennial. Nucl. Instrum. Meth. B 91, 22–29.

Ewing, R.C., Meldrum, A., Wang, L.-M., Weber, W.J., Corrales, L.R., 2003. Radiation effects in zircon. In: Hanchar, J.M., Hoskin, P.W.O. (Eds.), Zircon. Reviews in Mineralogy and Geochemistry, vol. 53. Miner. Soc. Am., Washington, DC, pp. 387–425.

Geisler, T., Pidgeon, R.T., Van Bronswijk, W., Pleysier, R., 2001. Kinetics of thermal recovery and recrystallization of partially metamict zircon: a Raman spectroscopic study. Eur. J. Mineral. 13, 1163–1176.

Geisler, T., Trachenko, K., Ríos, S., Dove, M.T., Salje, E.K.H., 2003. Impact of self-irradiation damage on the aqueous durability of zircon ($ZrSiO_4$): implications for its suitability as a nuclear waste form. J. Phys. Condens. Matter 15, L597–L605.

Ginster, U., Reiners, P.W., Farley, K.A., Nasdala, L., Chanmuang, N.C., 2018. Effects of radiation damage accumulation and annealing on He diffusion in zircon. In: 16th International Conference on Thermochronology, Quedlinburg, Germany, September, 2018. Conference abstracts, p. 69.

Ginster, U., Reiners, P.W., Nasdala, L., Chanmuang, N.C., 2019. Annealing kinetics of radiation damage in zircon. Geochim. Cosmochim. Acta 249, 225–246.

Gombosi, D.J., Garver, J.I., Baldwin, S.L., 2014. On the development of electron microprobe zircon fission-track geochronology. Chem. Geol. 363, 312–321.

Griffin, W.L., Powell, W.J., Pearson, N.J., O'Reilly, S.Y., 2008. Glitter: Data reduction software for laser ablation ICP-MS. In: Sylvester, P.J. (Ed.), Laser Ablation ICP–MS in the Earth Sciences: Current Practices and Outstanding Issues. Short Course Series, vol. 40. Miner. Ass. Canada, pp. 308–311.

Guenthner, W.R., Reiners, P.W., Ketcham, R.A., Nasdala, L., Giester, G., 2013. Helium diffusion in natural zircon: Radiation damage, anisotropy, and the interpretation of zircon (U–Th)/He thermochronology. Amer. J. Sci. 313, 145–198.

Guenthner, W.R., Reiners, P.W., Chowdhury, U., 2016. Isotope dilution analysis of Ca and Zr in apatite and zircon (U–Th)/He chronometry. Geochem. Geophys. Geosyst. 17, 1623–1640.

Hanchar, J.M., Finch, R.J., Hoskin, P.W.O., Watson, E.B., Cherniak, D.J., Mariano, A.N., 2001. Rare earth elements in synthetic zircon: part 1. Synthesis, and rare earth element and phosphorus doping. Am. Mineral. 86, 667–680.

Hazen, R.M., Finger, L.W., 1979. Crystal structure and compressibility of zircon at high pressure. Am. Mineral. 64, 196–201.

Holland, H.D., Gottfried, D., 1955. The effect of nuclear radiation on the structure of zircon. Acta Crystallogr. 8, 291–300.

Horie, K., Hidaka, H., Gauthier-Lafaye, F., 2006. Elemental distribution in zircon: alteration and radiation-damage effects. Phys. Chem. Earth 31, 587–592.

Hurley, P.M., 1954. The helium age method and the distribution and migration of helium in rocks. In: Faul, H. (Ed.), Nuclear Geology. Wiley, New York, pp. 301–329.

Huyskens, M.H., Zink, S., Amelin, Y., 2016. Evaluation of temperature-time conditions for the chemical abrasion treatment of single zircons for U–Pb geochronology. Chem. Geol. 438, 25–35.

Jackson, S.E., Pearson, N.J., Griffin, W.L., Belousova, E.A., 2004. The application of laser ablation-inductively coupled plasma-mass spectrometry to in situ U-Pb zircon geochronology. Chem. Geol. 211, 47–69.

Jochum, K.P., Weis, U., Stoll, B., Kuzmin, D., Yang, Q., Raczek, I., Jacob, D.E., Stracke, A., Birbaum, K., Frick, D.A., Günther, D., Enzweiler, J., 2011. Determination of reference values for NIST SRM 610–617 glasses following ISO guidelines. Geostand. Geoanal. Res. 35, 397–429.

Kennedy, A.K., 2000. The search for new zircon standards for SIMS. In: Woodhead, J.D., Hergt, J.M., Noble, W.P. (Eds.), Beyond 2000, New Frontiers in Isotope Geoscience (Incorporating ACOG 4): Abstracts and Proceedings. Lorne, Australia, January 30–February 4, 2000, pp. 109–111. ISBN 0734017723.

King, H.E., Finger, L.W., 1979. Diffracted beam crystal centering and its application to high-pressure crystallography. J. Appl. Crystallogr. 12, 374–378.

Kolesov, B.A., Geiger, C.A., Armbruster, T., 2001. The dynamic properties of zircon studied by single-crystal X-ray diffraction and Raman spectroscopy. Eur. J. Mineral. 13, 939–948.

Krogh, T.E., 1982. Improved accuracy of U-Pb zircon ages by the creation of more concordant systems using an air abrasion technique. Geochim. Cosmochim. Acta 46, 637–649.

Krogh, T.E., 1993. High precision U–Pb ages for granulite metamorphism and deformation in the Archean Kapuskasing structural zone, Ontario: implications for structure and development of the lower crust. Earth Planet. Sci. Lett. 119, 1–18.

Krogh, T.E., Davis, G.L., 1975. Alteration in zircons and differential dissolution of altered and metamict zircon. Carnegie I. Wash. 74, 619–623.

Kröner, A., Williams, I.S., Compston, W., Baur, N., Vitanage, P.W., Perera, L.R.K., 1987. Zircon ion-microprobe dating of high-grade rocks in Sri Lanka. J. Geol. 95, 775–791.

Lenz, C., Nasdala, L., 2015. A photoluminescence study of REE^{3+} emissions in radiation-damaged zircon. Am. Mineral. 100, 1123–1133.

Mattinson, J.M., 1994. A study of complex discordance in zircons using step-wise dissolution techniques. Contrib. Mineral. Petrol. 116, 117–129.

Mattinson, J.M., 2005. Zircon U–Pb chemical abrasion (CA-TIMS) method: combined annealing and multi-step dissolution analysis for improved precision and accuracy of zircon ages. Chem. Geol. 220, 47–56.

Mattinson, J.M., 2011. Extending the Krogh legacy: development of the CA–TIMS method for zircon U–Pb geochronology. Can. J. Earth Sci. 48, 95–105.

Mattinson, J.M., Nasdala, L., Lengauer, C., Wirth, R., 2007. Inside CA-TIMS zircon analysis; the interplay among natural radiation damage, annealing, solubility, and U-

Pb isotopic systematics. EOS T Am. Geophys. Un. 88 (52). Fall Meeting Suppl, abstr. V31G–06.

Montario, M.J., Garver, J.I., 2009. The thermal evolution of the Grenville Terrane revealed through U-Pb and fission-track analysis of detrital zircon from Cambro-Ordovician quartz arenites of the Potsdam and Galway Formations. J. Geol. 117, 595–614.

Moreira, P.A.F.P., Devanathan, R., Yu, J., Weber, W.J., 2009. Molecular-dynamics simulation of threshold displacement energies in zircon. Nucl. Instrum. Meth. B 267, 3431–3436.

Moreira, P.A.F.P., Devanathan, R., Weber, W.J., 2010. Atomistic simulation of track formation by energetic recoils in zircon. J. Phys. Condens. Matter 22, 395008.

Mundil, R., Metcalfe, I., Ludwig, K.R., Renne, P.R., Oberli, F., Nicoll, R.S., 2001. Timing of the Permian–Triassic biotic crisis: implications from new zircon U/Pb age data (and their limitations). Earth Planet. Sci. Lett. 197, 131–145.

Mundil, R., Ludwig, K.R., Metcalfe, I., Renne, P.R., 2004. Age and timing of the Permian mass extinctions: U/Pb dating of closed-system zircons. Science 305, 1760–1763.

Murakami, T., Chakoumakos, B.C., Ewing, R.C., Lumpkin, G.R., Weber, W.J., 1991. Alpha-decay event damage in zircon. Am. Mineral. 76, 1510–1532.

Mursic, Z., Vogt, T., Frey, F., 1992. High-temperature neutron powder diffraction study of ZrSiO₄ up to 1900 K. Acta Crystallogr. B 48, 584–590.

Nasdala, L., Wenzel, M., Vavra, G., Irmer, G., Wenzel, T., Kober, B., 2001. Metamictisation of natural zircon: accumulation versus thermal annealing of radioactivity-induced damage. Contrib. Mineral. Petrol. 141, 125–144.

Nasdala, L., Lengauer, C.L., Hanchar, J.M., Kronz, A., Wirth, R., Blanc, P., Kennedy, A.K., Seydoux-Guillaume, A.-M., 2002. Annealing radiation damage and the recovery of cathodoluminescence. Chem. Geol. 191, 121–140.

Nasdala, L., Reiners, P.W., Garver, J.I., Kennedy, A.K., Stern, R.A., Balan, E., Wirth, R., 2004. Incomplete retention of radiation damage in zircon from Sri Lanka. Am. Mineral. 89, 219–231.

Nasdala, L., Hofmeister, W., Norberg, N., Mattinson, J.M., Corfu, F., Dörr, W., Kamo, S.L., Kennedy, A.K., Kronz, A., Reiners, P.W., Frei, D., Kosler, J., Wan, Y., Götze, J., Häger, T., Kröner, A., Valley, J.W., 2008. Zircon M257 – A homogeneous natural reference material for the ion microprobe U-Pb analysis of zircon. Geostand. Geoanal. Res. 32, 247–265.

Nasdala, L., Hanchar, J.M., Rhede, D., Kennedy, A.K., Váczi, T., 2010. Retention of uranium in complexly altered zircon: an example from Bancroft, Ontario. Chem. Geol. 269, 290–300.

Nasdala, L., Corfu, F., Valley, J.W., Spicuzza, M.J., Wu, F.-Y., Li, Q.-L., Yang, Y.-H., Fisher, C., Münker, C., Kennedy, A.K., Reiners, P.W., Kronz, A., Wiedenbeck, M., Wirth, R., Chanmuang, C., Zeug, M., Váczi, T., Norberg, N., Häger, T., Kröner, A., Hofmeister, W., 2016. Zircon M127 – A reference material for U-Pb combined with hafnium, oxygen and, potentially, lithium isotope analysis. Geostand. Geoanal. Res. 40, 457–475.

Nasdala, L., Akhmadaliev, S., Artac, A., Chanmuang, N.C., Habler, G., Lenz, C., 2018a. Irradiation effects in monazite–(Ce) and zircon: Raman and photoluminescence study of Au-irradiated FIB foils. Phys. Chem. Miner. 45, 855–871.

Nasdala, L., Corfu, F., Schoene, B., Tapster, S.R., Wall, C.J., Schmitz, M.D., Ovtcharova, M., Schaltegger, U., Kennedy, A.K., Kronz, A., Reiners, P.W., Yang, Y.-H., Wu, F.-Y., Gain, S.E.M., Griffin, W.L., Szymanowski, D., Chanmuang, N.C., Ende, M., Valley, J.W., Spicuzza, M.J., Wanthanachaisaeng, B., Giester, G., 2018b. GZ7 and GZ8 – two zircon references for SIMS U–Pb geochronology. Geostand. Geoanal. Res. 42, 431–457.

Oliver, W.C., McCallum, J.C., Chakoumakos, B.C., Boatner, L.A., 1994. Hardness and elastic modulus of zircon as a function of heavy-particle irradiation dose: II. Pb-ion implantation damage. Rad. Effects Defects Solids 132, 131–141.

Pidgeon, R.T., Furfaro, D., Kennedy, A.K., Nemchin, A.A., van Bronswijk, W., 1994. Calibration of zircon standards for the Curtin SHRIMP II. In: Lanphere, M.A., Dalrymple, G.B., Turrin, B.D. (Eds.), Abstracts of the Eighth International Conference on Geochronology, Cosmochronology and Isotope Geology. U.S. Geol. Surv. Circular 1107, p. 251.

Presby, H.M., Brown, W.L., 1974. Refractive index variations in proton-bombarded fused silica. Appl. Phys. Lett. 24, 511–513.

Pruneda, J.M., Archer, T.D., Artacho, E., 2004. Intrinsic point defects and volume swelling in ZrSiO₄ under irradiation. Phys. Rev. B 70, 104111.

Reiners, P.W., 2005. Zircon (U–Th)/He thermochronometry. In: Reiners, P.W., Ehlers, T. A. (Eds.), Low-Temperature Thermochronology: Techniques, Interpretations, and Applications. Reviews in Mineralogy and Geochemistry, vol 58. Miner. Soc. Am., Chantilly, VA, pp. 151–179.

Ríos, S., Salje, E.K.H., 1999. Diffuse x-ray scattering from weakly metamict zircon. J. Phys. Condens. Matter 11, 8947–8956.

Ríos, S., Malcherek, T., Salje, E.K.H., Domeneghetti, C., 2000a. Localized defects in radiation-damaged zircon. Acta Crystallogr. B 56, 947–952.

Ríos, S., Salje, E.K.H., Zhang, M., Ewing, R.C., 2000b. Amorphization in zircon: evidence for direct impact damage. J. Phys. Condens. Matter 12, 2401–2412.

Robinson, K., Gibbs, G.V., Ribbe, P.H., 1971. The structure of zircon: a comparison with garnet. Am. Mineral. 56, 782–790.

Rossmann, M.G., 1979. Processing oscillation diffraction data for very large unit cells with an automatic convolution technique and profile fitting. J. Appl. Crystallogr. 12, 225–238.

Salje, E.K.H., Chrosch, J., Ewing, R.C., 1999. Is "metamictization" of zircon a phase transition? Am. Mineral. 84, 1107–1116.

Santosh, M., Tsunogae, T., Malaviarachchi, S.P.K., Zhang, Z.M., Ding, H.X., Tang, L., Dharmapriya, P.L., 2014. Neoproterozoic crustal evolution in Sri Lanka: insights from petrologic, geochemical and zircon U–Pb and Lu–Hf isotopic data and implications for Gondwana assembly. Precambrian Res. 255, 1–29.

Seydoux-Guillaume, A.-M., Wirth, R., Nasdala, L., Gottschalk, M., Montel, J.M., Heinrich, W., 2002. An XRD, TEM and Raman study of experimentally annealed natural monazite. Phys. Chem. Miner. 29, 240–253.

Sheldrick, G.M., 2015. Crystal structure refinement with SHELXL. Acta Crystallogr. C 71, 3–8.

Tokuda, M., Yoshiasa, A., Kojitani, H., Hashimoto, S., Uehara, S., Mashimo, T., Tobase, T., Akaogi, M., 2019. The importance of cation–cation repulsion in the zircon–reidite phase transition and radiation-damaged zircon. Mineral. Mag. 83, 561–567.

Trachenko, K., Dove, M.T., Salje, E.K.H., 2002. Structural changes in zircon under a-decay irradiation. Phys. Rev. B 65, 180102.

Trachenko, K., Dove, M.T., Geisler, T., Todorov, I., Smith, B., 2004. Radiation damage effects and percolation theory. J. Phys. Condens. Matter 16, S2623–S2627.

Váczi, T., 2014. A new, simple approximation for the deconvolution of instrumental broadening in spectroscopic band profiles. Appl. Spectrosc. 68, 1274–1278.

Váczi, T., Nasdala, L., Wirth, R., Mehofer, M., Libowitzky, E., Häger, T., 2009. On the breakdown of zircon upon "dry" thermal annealing. Mineral. Petrol. 97, 129–138.

Vaz, J.E., Senftle, F.E., 1971. Thermoluminescence study of the natural radiation damage in zircon. J. Geophys. Res. 76, 2038–2050.

Weber, W.J., 1990. Radiation-induced effects and amorphization in zircon. J. Mater. Res. 5, 2687–2697.

Weber, W.J., Ewing, R.C., Wang, L.-M., 1994. The radiation-induced crystalline-to-amorphous transition in zircon. J. Mater. Res. 9, 688–698.

Weber, W.J., Ewing, R.C., Catlow, C.R.A., Diaz de la Rubia, T., Hobbs, L.W., Kinoshita, C., Matzke, H., Motta, A.T., Nastasi, M., Salje, E.K.H., Vance, E.R., Zinkle, S.J., 1998. Radiation effects in crystalline ceramics for the immobilization of high-level nuclear waste and plutonium. J. Mater. Res. 13, 1434–1484.

Welberry, T.R., Weber, T., 2016. One hundred years of diffuse scattering. Crystallogr. Rev. 22, 2–78.

Wirth, R., Langer, K., Platonov, A.N., 2001. TEM study of a chromium-bearing kyanite from mantle xenolith: evidence for an alumina-rich exsolution precursor phase. Eur. J. Mineral. 13, 311–318.

Zamyatin, D.A., Shchapova, Y.V., Votyakov, S.L., Nasdala, L., Lenz, C., 2017. Alteration and chemical U-Th-total Pb dating of heterogeneous high-uranium zircon from a pegmatite from the Aduiskii Massif, Middle Urals, Russia. Mineral. Petrol. 111, 475–497.

Zeug, M., Nasdala, L., Wanthanachaisaeng, B., Balmer, W.A., Corfu, F., Wildner, M., 2018. Blue zircon from Ratanakiri, Cambodia. J. Gemmol. 36 (2), 112–132.

Zhang, M., Salje, E.K.H., Farnan, I, Graeme-Barber, A., Daniel, P., Ewing, R.C., Clark, A. M., Leroux, H., 2000. Metamictization of zircon: Raman spectroscopic study. J. Phys. Condens. Matter 12, 1915–1925.